

EVIDENCE FOR DISTINCT COMPONENTS OF THE GALACTIC STELLAR HALO FROM 838 RR LYRAE STARS DISCOVERED IN THE LONEOS-I SURVEY

ANTONINO MICELI

Astronomy and Physics Departments, University of Washington, Box 351580, Seattle, WA 98195-1580 USA,
amiceli@astro.washington.edu

ARMIN REST

Cerro Tololo Inter-American Observatory, National Optical Astronomy Observatory, Casilla 603, LaSerena, Chile,
arest@ctio.noao.edu

CHRISTOPHER W. STUBBS

Department of Physics and Harvard-Smithsonian Center for Astrophysics, Harvard University, 17 Oxford Street, Cambridge, MA 02138
USA

SUZANNE L. HAWLEY

Astronomy Department, University of Washington, Box 351580, Seattle, WA 98195-1580 USA

KEM H. COOK

Lawrence Livermore National Laboratory, 7000 East Ave., Livermore, CA 94550 USA

EUGENE A. MAGNIER

University of Hawaii, Institute for Astronomy, 2680 Woodlawn Dr., Honolulu, HI 96822 USA

KEVIN KRISCIUNAS

University of Notre Dame, Department of Physics, 225 Nieuwland Science Hall, Notre Dame, IN 46556 USA

EDWARD BOWELL

Lowell Observatory, 1400 West Mars Hill Road, Flagstaff, AZ 86001 USA

AND

BRUCE KOEHN

Lowell Observatory, 1400 West Mars Hill Road, Flagstaff, AZ 86001 USA

Draft version October 23, 2018

ABSTRACT

We present 838 *ab*-type RR Lyrae stars from the Lowell Observatory Near Earth Objects Survey Phase I (LONEOS-I). These objects cover 1430 deg^2 and span distances ranging from 3-30kpc from the Galactic Center. Object selection is based on phased, photometric data with 28-50 epochs. We use this large sample to explore the bulk properties of the stellar halo, including the spatial distribution. The period-amplitude distribution of this sample shows that the majority of these RR Lyrae stars resemble Oosterhoff type I, but there is a significant fraction (26%) which have longer periods and appear to be Oosterhoff type II. We find that the radial distributions of these two populations have significantly different profiles ($\rho_{OoI} \sim R^{-2.26 \pm 0.07}$ and $\rho_{OoII} \sim R^{-2.88 \pm 0.11}$). This suggests that the stellar halo was formed by at least two distinct accretion processes and supports dual-halo models.

Subject headings: galaxies: structure—galaxies: halos—galaxies: individual (MWG)

1. INTRODUCTION

A major goal of modern astrophysics is to understand the physical processes by which galaxies form, and to place galaxy formation in the context of models for the evolution of large-scale structure in the Universe. The advent of wide-field CCD cameras has now made it possible to survey large samples of Galactic stellar populations, and therefore to study the structure of our Galaxy as a whole. While keeping in mind that the Galaxy may not always be representative of (spiral) galaxies in gen-

eral, the study of our Galaxy is now a fruitful avenue for the detailed exploration of galactic structure, providing the empirical basis for differentiating between formation models.

RR Lyrae stars are horizontal branch stars which lie in the instability strip. They represent a late stage of stellar evolution, and as such form an old stellar population that can be used to study the early stages of galaxy formation. RR Lyrae stars have a long history as tracers of Galactic structure (Kinman et al. 1966; Oort & Plaut

1975; Hawkins 1984; Saha 1985). They are also relatively easy to identify from their colors and variability, enabling the formation of samples with little contamination. Suntzeff et al. (1991) estimate the number of field RR Lyrae in the Galactic halo to be about 85,000, but less than 8,000 have been discovered, including those in the bulge and thick disk (e.g., Heck 1988). Further, their absolute magnitudes (for RR Lyrae *ab*-types) have been measured to better than 0.1 magnitudes using robust statistical parallax (Layden et al. 1996) and direct parallax techniques (Benedict et al. 2002). However, RR Lyrae stars do have a disadvantage. The relative abundance of RR Lyrae stars depends on the horizontal branch morphology of the RR Lyrae progenitor system. Thus, they may not reveal the entire history of Galactic formation. Overall, RR Lyrae stars are an incisive probe of the halo field population and may provide useful insights on Galactic formation. In recent years, several sky surveys have discovered large numbers of Galactic RR Lyrae over large fractions of the sky, e.g. SDSS (Ivezić et al. 2000), QUEST (Vivas & Zinn 2006), and NSVS (Kinemuchi et al. 2006). The SDSS and QUEST surveys have shown that RR Lyrae can be used to find and trace the remnants of accreted satellite galaxies in the Galaxy.

RR Lyrae also have been well cataloged and studied in the globular clusters (e.g., Clement et al. 2001). In particular, globular clusters fall into two broad groups based on the mean periods of their RRab stars and on their RRc fraction, with Oosterhoff I (OoI) clusters having shorter mean periods and lower RRc content compared to Oosterhoff II (OoII) clusters (Oosterhoff 1939). In addition, these two classes populate distinct regions in period-amplitude space. There are certain stellar systems (most Local Group dwarf spheroidals) which cannot be classified as OoI nor OoII, but rather exhibit period-amplitude distributions which fall between OoI and OoII. These are referred to as intermediate. We can examine Galactic stellar halo RR Lyrae in a similar manner to determine their Oosterhoff classification. Suntzeff et al. (1991) found OoI and OoII components in field RR Lyrae stars, but no intermediate Oo component (i.e., the Oosterhoff “gap”). The origin of this Oosterhoff effect has been studied intensively (e.g., Sandage et al. 1981; Lee et al. 1990; Lee & Carney 1999). The Oosterhoff classification may either indicate an age difference or a metallicity difference. Regardless, the Oosterhoff classification of the RR Lyrae in the Galactic stellar halo will provide insights into its formation history.

In this paper, we present new results from the LONEOS - I RR Lyrae survey. Using 838 RR Lyrae stars discovered from the LONEOS - I survey, we will investigate their distribution in the stellar halo out to distances of 30 kpc, as a function of Galactic position. In Section 2, we introduce the LONEOS - I variability survey and discuss the photometric pipeline. In Section 3, we present the LONEOS - I RR Lyrae sample and discuss the selection process and detection efficiency. In Section 4, we discuss the properties of the LONEOS - I RR Lyrae stars. Finally, we discuss the implications for Galactic formation and look to the future.

2. LONEOS - I VARIABILITY SURVEY

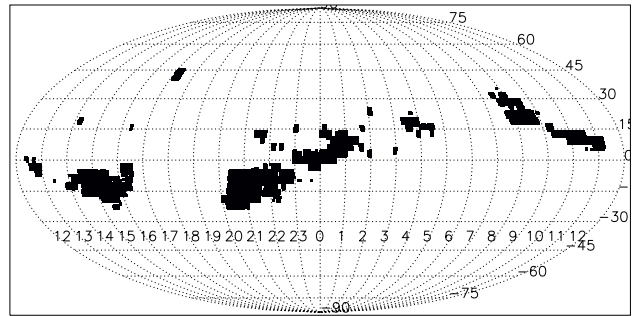


FIG. 1.— The black regions indicate subfields of LONEOS - I survey data with at least 28 good quality images. These fields are used for our RR Lyrae star analysis in this paper. This area covers 1430 deg^2 on the sky. The equatorial coordinates of the subfields are displayed using a Mollweide projection.

The Lowell Observatory Near Earth Object Survey (LONEOS) (Bowell et al. 1995) has as its primary goal the detection of potentially hazardous asteroids. Situated on the Anderson Mesa outside Flagstaff, Arizona, LONEOS is carried out with a 0.6m Schmidt telescope. During the first two years of operation, imaging was done with a camera constructed at the University of Washington (Diercks et al. 1995), with a single 2k x 4k unfiltered CCD (5 sq. deg. FOV with $2.67''/\text{pixels}$) (LONEOS - I). Under optimal conditions, LONEOS can image up to 1000 square degrees per night, multiple times. The LONEOS - I survey imaged fields three times a night with 60 second exposure times. Fields are re-observed at least one other time about one lunation later. LONEOS - I camera uses no bandpass filter, but the data can be transformed to a standard photometric system using external datasets. The LONEOS - I camera can reach a depth of $R \sim 18.5$.

Besides searching for moving objects, this dataset can be used to search for temporal variability, specifically of stellar objects. Data from LONEOS have been used to construct a stellar temporal variability database, from which we extracted candidate RR Lyrae stars. The cadence of LONEOS observations makes them well suited to detect short-term variability (e.g., RR Lyrae, binaries, CVs), and long-term variability (e.g., QSOs).

The LONEOS - I photometric variability database discussed in this paper consists of photometric data obtained between 1998 - 2000. It covers a large fraction of the sky, much of it imaged in multiple epochs (see Figure 1). The LONEOS - I dataset that we will analyze in this paper consists of 1430 deg^2 with at least 28 epochs.

2.1. Image Reduction Pipeline

The LONEOS - I image reduction pipeline consists of several steps. Basic CCD processing (bias, flat-field correction) is followed by object detection using the photometry program DoPhot (Schechter et al. 1993). Bookkeeping is accomplished by automatic merging of the DoPhot output file with the FITS header of each parent image to produce a self-describing and self-contained output file. These output files are entered into a database (broken down by region on the sky) where the primary indexing is based on image position (RA, DEC). The relative and absolute photometry is performed at the database level. We divide each field into subfields, and relative photometry is performed on these subfields. We tie the

LONEOS - I absolute photometry to an external catalog. Details are presented in later sections. Access tools are used to search the database and apply variability detection algorithms. We have developed a set of robust statistics which are used to discriminate between long and short term variables in the timeseries data. It should be noted that we do not attempt to perform accurate photometry of extended objects. The database should be strictly used for stellar objects. For details of the data reduction pipeline see Rest (2002).

2.1.1. Photometry

The photometric calibration can be separated into two independent parts: relative photometry and absolute photometry. For identification and classification of variable objects, relative photometry suffices. Since LONEOS uses an unfiltered system, we must rely on external datasets to tie the relative magnitudes to a standard photometric system. We outline the procedure in this section.

For an image taken at a given time t and airmass $a(t)$ through a filter X , the apparent magnitude $m(t, s)$ of a star s with color $X - Y$ (e.g. $X - Y = B - V$) can be written as

$$m(t, s) = m_{instr}(t, s) + A_X(t) + c_1 * a(t) + c_2 * (X - Y) * a(t) + c_3 * (X - Y) + m_0(1)$$

Here $m_{instr}(t, s)$ is the instrumental magnitude with an error of $\sigma_{instr}(t, s)$, $A_X(t)$ is the extinction due to clouds (assuming 'grey' extinction), c_1 and c_2 are the grey and color-dependent airmass extinction coefficients, respectively. For our purposes, since we are interested in the photometry of only one type of star, we can set $(X - Y)$ to a constant, and include c_2 in c_1 and c_3 in m_0 . LONEOS takes images of fields with generally low airmass (76% of images have airmass less than 1.5 with a mean airmass of 1.3). Therefore, the second order term depending on color and airmass is very small anyway. We group all image-dependent terms into $m_{cal}(t) = A_X(t) + c_1 * a(t)$ and

$$m(t, s) = m_{instr}(t, s) + m_{cal}(t) + m_0. \quad (2)$$

A wide field-of-view or strong PSF distortions of the optical system can cause systematic variations in the photometry across the image. We divide each LONEOS field (i.e. 2k x 4k) into 50 square *subfields*, each 0.304 degrees on a side. This subfield size is large enough to include a sufficiently large number of stars to perform the photometry, but small enough to avoid systematic problems (e.g., Flat fielding errors, clouds, etc) across the wide FOV of the camera.

2.1.2. Relative Photometry

We define the relative magnitude $m_{rel}(t, s)$ and the time-averaged relative magnitude $\bar{m}_{rel}(s)$ of the star s as:

$$m_{rel}(t, s) = m_{instr}(t, s) + m_{cal}(t), \quad (3)$$

$$\bar{m}_{rel}(s) = \sum_t \frac{m_{rel}(t, s)}{\sigma_{instr}^2(t, s)}, \quad (4)$$

$$\bar{\sigma}_{rel}^{-2}(s) = \sum_t \sigma_{instr}^{-2}(t, s). \quad (5)$$

We take the following approach to perform relative photometric calibration: calculate the time-averaged magnitude for each star, then adjust $m_{cal}(t)$ in each subfield, so that on the average the deviation from single star measurements to the time-averaged star magnitude is minimized. The function that is minimized is:

$$\chi^2 = \sum_{t,s} (\bar{m}_{rel}(s) - m_{rel}(t, s))^2 / \sigma^2(t, s) + \sum_t m_{cal}(t), \quad (6)$$

$$\sigma^2(t, s) = \bar{\sigma}_{rel}^2(s) + \sigma_{instr}^2(t, s), \quad (7)$$

where $m_{cal}(t)$ are the free parameters. Note that without the second term, the χ^2 is degenerate to the addition of a constant to the $m_{cal}(t)$ vector. Therefore we add the second term which is quadratic in the degenerate direction. Hence our solution has $\sum_t m_{cal}(t) = 0$. We also add 0.02 magnitudes in quadrature to $\sigma_{instr}(t, s)$ to take into account systematic error. This is intended to compensate for the fact that DoPhot is known to underestimate photometric errors at the bright end, where the error is dominated by systematics rather than Poisson noise. These systematics include flat fielding errors, PSF variations, and the limited accuracy of the PSF model. Stars for which the reduced χ_s^2 of their lightcurve exceeds 2.5 are flagged as potentially variable and excluded from the set of stars used to fit $m_{cal}(t)$, with

$$\chi_s^2 = 1 / (N_t - 1) \sum_t (\bar{m}_{rel}(s) - m_{rel}(t, s))^2 / \sigma^2(t, s). \quad (8)$$

Here N_t is the number of images. Similarly, we exclude images for which their reduced χ_t^2 exceeds 1.5, with

$$\chi_t^2 = 1 / (N_s - 1) \sum_s (\bar{m}_{rel}(s) - m_{rel}(t, s))^2 / \sigma^2(t, s). \quad (9)$$

In addition, we exclude images for which more than 20% of the star measurements $m_{rel}(t, s)$ deviate by more than 3 σ from their time-averaged magnitude $\bar{m}_{rel}(s)$. This process is repeated iteratively until the $m_{cal}(t)$ vector values for each subfield do not change significantly.

2.1.3. Absolute Photometry: Tying LONEOS Photometry to External Datasets

Since LONEOS uses an unfiltered camera, we must use external datasets to tie LONEOS photometry to a standard photometric system. There exist datasets of calibrated photometry over large portions of the sky. We use the Guide Star Catalog 2.2 (Space Telescope Science Institute & Osservatorio Astronomico di T 2001) (hitherto, referred to as GSC). GSC is complete to 18.5 photographic F-band, and Tycho 2 photometry is used for bright sources. Thus, the GSC magnitude range matches well to LONEOS - I. The procedure to tie LONEOS relative photometry to GSC is similar to the relative photometry algorithm. We restrict the range of color ($-1.1 < (M_{GSC-J} - M_{GSC-F}) < 1.5$) for the GSC stars to be similar to colors of RR Lyrae, which are the focus of this work. The spectral response of the LONEOS - I camera system matches closest to the GSC F passband. Initially, LONEOS - I photometry is tied to GSC F, which we refer to as $M_{LONEOS-F}$ with error

σ_{LONEOS_F} . Combining Equations 2, 3 and 4, we define the time-averaged apparent magnitude $\bar{M}_{LONEOS_F}(s)$ of the star s in each subfield t as:

$$\bar{M}_{LONEOS_F}(s) = \bar{m}_{rel}(s) + m_{0,GSC_F}, \quad (10)$$

$$\bar{\sigma}(s) = \bar{\sigma}_{rel}^2(s) + \sigma_{m_{0,GSC_F}}^2. \quad (11)$$

We determine the free parameter m_{0,GSC_F} and its error $\sigma_{m_{0,GSC_F}}$ for a given subfield by minimizing

$$\chi^2 = \sum_s (M_{GSC_F}(s) - \bar{M}_{LONEOS_F}(s))^2 / (\sigma_{GSC_F}^2 + \bar{\sigma}_{rel}^2(s))$$

where the sum is taken over the stars in a given image. Once m_0 is determined for each subfield, the LONEOS magnitude tied to GSC F for a given star s , in that subfield is:

$$M_{LONEOS_F}(t, s) = m_{instr}(t, s) + m_{cal}(t) + m_{0,GSC_F} \quad (13)$$

However, the absolute magnitude of RR Lyrae have been measured in V . We use photometry from SDSS Data Release 3 (DR3) (Abazajian et al. 2005) to convert M_{LONEOS_F} to a V -based system, in this case a synthetic SDSS-based magnitudes ($V_{SDSS} = r + 0.44(g - r) - 0.02$ (Ivezić et al. 2005)). All magnitudes have been corrected for Galactic extinction using Schlegel et al. (1998). The residual of M_{LONEOS_F} and V_{SDSS} as a function SDSS color, $g - r$, has a clear trend (Figure 2). Thus, we must restrict the range of SDSS color used to an empirical offset between M_{LONEOS_F} and V_{SDSS} . Stars in the DR3 with colors of RR Lyrae (Ivezić et al. 2005) are matched to LONEOS - I stars ($0.99 < u - g < 1.28$, $-0.11 < g - r < 0.31$, $-0.13 < r - i < 0.2$, $-0.19 < i - z < 0.23$). A total of 40,180 SDSS DR3 stellar objects in this color range were matched to LONEOS - I objects. Using LONEOS - I timeseries, we reject stars with signs of variability. We see that there is an offset, $M_{LONEOS_F} - V_{SDSS} = -0.32$, with a scatter of 0.13. All subsequent LONEOS - I photometry in this work is tied to the V_{SDSS} system via this offset. The final transformation is:

$$M_{LONEOS\ V} = [M_{LONEOS\ F} - A_{GSCF} \times E(B-V)] + 0.32, \quad (14)$$

where $A_{GSCF} = 2.65$ is the extinction coefficient and $E(B-V)$ is the reddening. This transformation is only valid for stars with colors similar to those of RR Lyrae stars.

The distribution of the residuals is approximately Gaussian in the core, but there are long tails in the distribution, most likely due to plate-to-plate systematic errors in the GSC photographic sky survey. Figure 3 shows the residual of M_{LONEOS_F} and V_{SDSS} as a function of Right Ascension. One can clearly see systematic errors as a function of RA. These are on the scale of Schmidt plate size (6 degrees). However, these large errors occur over only a small fraction of the sky. 0.98% of the stars have residuals greater than 3σ from the mean compared to 0.3% for a Gaussian distribution. Since the survey area which we will analyze is large, these errors do not affect the statistical properties of our RR Lyrae sample.

3. LONEOS - I AB-TYPE RR LYRAE STAR CATALOG

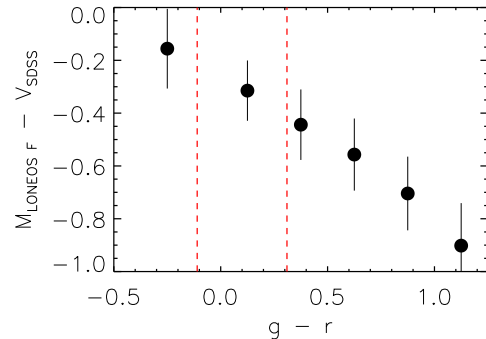


FIG. 2.— The residual between LONEOS - I magnitudes (tied to GSC2 F) and V_{SDSS} as a function of SDSS color, $g - r$. The two dashed vertical lines indicate the color range typical for RR Lyrae. In this range, we see that there is an offset, $M_{LONEOS_F} - V_{SDSS} = -0.32$, with an RMS of 0.13.

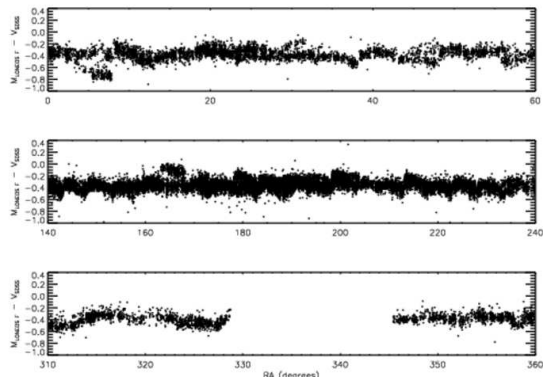


FIG. 3.— The residual between LONEOS magnitudes (tied to GSC2) and SDSS as a function of RA for equatorial region. One can see the systematic difference between different POSS plates.

In this section, we will describe the selection of RR Lyrae using LONEOS - I data, and present the LONEOS - I RR Lyrae star catalog. This currently represents the largest single sample of halo RR Lyrae stars. In addition, we discuss the detection efficiency of our selection process and the completeness of our sample.

3.1. Selection of LONEOS - I RR Lyrae Stars

The selection of the RR Lyrae was solely based on LONEOS - I temporal photometric data. No color information was used. We restrict our search to fields with more than 28 good quality images. This amounts to 1430 deg^2 of coverage. The median number of images is 31. We impose a set of variability criteria which first identifies short-term variable stars, and then analyzes the morphology of the phased light curves. We limit our search to ab -type RR Lyrae, since it is difficult to detect efficiently the c -type RR Lyrae given our temporal sampling. In order to accurately determine our detection efficiency, we did not directly rely on visual inspection to produce our sample, but used a series of cuts which aim to maximize the detection of RR Lyrae in an objective manner. Below, we outline our selection criteria (see Figure 4).

To reject non-variables and/or low amplitude variables, we made two variability cuts on the timeseries:

- We first looked at the spread of the measured

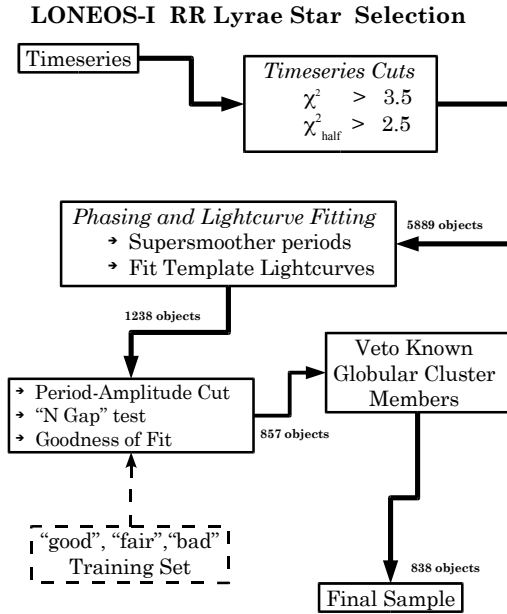


FIG. 4.— LONEOS - I RR Lyrae flow chart indicate the selection process and criteria used in the analysis of this paper.

magnitudes about the average magnitude, normalized by the photometric error, which is a reduced χ^2 . We define this statistic as: $\chi^2 = \frac{1}{N-1} \sum_{i=1}^N \frac{(m_i - \bar{m})^2}{\sigma_i^2}$, where N is the number of observations, m_i is the magnitude of the i^{th} observation, \bar{m} is the mean magnitude, and σ_i is the photometric error of the i^{th} observation. χ^2 gives a measure of the variability over the entire timeseries. We rejected stars with $\chi^2 < 3.5$. This predominantly rejected small amplitude variables.

- We divided the timeseries into two segments, each containing half the data points, and calculated χ^2 for both halves. We required $\chi^2 > 2.5$ for both halves of the timeseries. This rejects objects that are aperiodic or that have inflated χ^2 from occasional outliers.

A total of 5889 objects satisfied these cuts. In order to identify RR Lyrae stars in this sample, we search for a periodic signal in these timeseries. In addition, we must classify Period-folded light curves. However, the LONEOS - I sampling is not sufficient to use sophisticated classification methods, such as Fourier decomposition or machine learning methods. We use template light curves to distinguish RR Lyrae from other common light curves, such as sinusoidal variables and eclipsing binaries. We use the nine templates from Layden (1998), based on high quality light curves of bright RR Lyrae stars which have been averaged. Six templates are *ab*-type RR Lyrae stars. In addition, there are single templates for *c*-type RR Lyrae, for a sinusoid, and for a W UMa-type contact binary (Figure 5). There are a sizable number of contact binaries in the LONEOS - I database. The fundamental mode RR Lyrae *ab*-type can be broken down into two different categories, type *a* and *b* (i.e., “Bailey” type). Bailey type *a* objects have flatter bottoms, and the Bailey type *b* have a sawtooth shape. The first six templates represent typical RR Lyrae light curve shapes

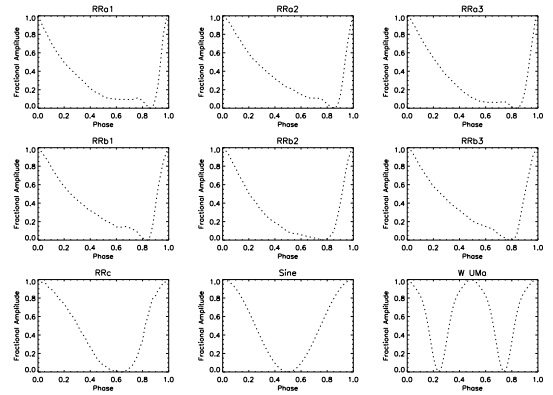


FIG. 5.— The best four periods from the supersmoother are fit to these nine templates. The mean magnitude, phase and amplitude are free parameters in the fit. These nine templates are taken from Layden (1998). The first six are *ab*-type RR Lyrae which were obtained from the averaging of high-quality light curves. The last three include a *c*-type RR Lyrae, a sine wave, and W UMa contact binary.

for type *a* and *b* with three different rise times (i.e., the phase interval between maximum and minimum light).

We used a supersmoother routine (Reimann 1994) to obtain a set of four best periods. The supersmoother is a variable span smoother, where the best span is chosen using a cross-validation technique. It was developed for the MACHO experiment (Alcock et al. 1995). We have tested other standard routines, such as Phase Dispersion Minimization (Stellingwerf 1978) and Lomb-Scargle periodogram (Scargle 1982); these alternative algorithms provide comparable results to the supersmoother. The supersmoother makes no assumptions regarding the morphology of the light curve. As a consequence, the supersmoother’s best period may not represent a physically realistic light curve. In addition, we have found that light curves with outlying data points adversely affect the supersmoother’s figure of merit for smoothness.

We limited the period search to range between 0.25 and 0.9 days. Our results were not affected if the search is extended to 2.0 days. In order to break degeneracies between the four best periods returned, we used a non-linear χ^2 minimization method to fit the phased data to our set of template light curves (Figure 5). The magnitude offset, phase and amplitude were free parameters in the template fitting. We required that the fit amplitudes be greater than 0.3 magnitudes. Each of the four periods was fit separately. The best period was selected by the quality of the template fit.

Objects were tentatively classified as *ab*-type RR Lyrae if convergence of the non-linear minimization was satisfied for the fits to one of the six *RRab* templates. We defer any template light curve goodness-of-fit cuts until later. Objects with best fits to the three non-*RRab* template light curves were discarded. A total of 1238 objects were classified as *ab*-type RR Lyrae. These objects were visually inspected and classified into three groups: “good”, “fair”, and “bad”. The criteria for the classifications included: goodness-of-fit to template light curve, and uniformity of data across phase. It is fairly easy to classify objects in the “good” and “bad” categories. The “fair” group includes objects where there was some ambiguity in the classification. These classifications were used as a training sample for further selection criteria.

The aim was to determine a totally automated set of selection criteria to maximize the selection of real RR_{ab} while minimizing contamination. This will facilitate the calculation of our detection efficiency. We developed the following criteria for quality of the light curves. First, we required that the fitted periods and amplitudes reside in the region of period-amplitude space where RR_{ab} are known to lie. This region was defined to contain the bulk of our “good” sample, and was large enough to encompass the range of metallicities and Oosterhoff groups associated with halo RR Lyrae stars. We are guided by the MACHO RR Lyrae period-amplitude distribution for the Galactic Bulge (Alcock et al. 1998), which contains a population of RR Lyrae stars with a wide range of metallicities. The region in period-amplitude space was defined as:

$$A < 1.5 \text{ magnitudes}, \quad (15)$$

$$A > 0.3 \text{ magnitudes}, \quad (16)$$

$$A > -5 \log(P) - 1 \text{ magnitudes}, \quad (17)$$

$$A < -5 \log(P) + 0.3 \text{ magnitudes}, \quad (18)$$

where periods are measured in days. Using the well-sampled light curves from Northern Sky Variability Survey (NSVS), Kinemuchi et al. (2006) found a population of ab -type RR Lyrae with shorter periods than the OoI group. Using light curve Fourier decomposition techniques, Kinemuchi et al. (2006) determined that this population was more metal-rich than the rest of the ROTSE-I sample. This population was identified as a metal-rich thick disk RR Lyrae star population. Our period-amplitude cut largely excludes this metal-rich thick disk RR Lyrae star population. A metal-weak thick disk RR Lyrae star population also likely exists, but this population smears with the OoI in the period-amplitude diagram. Thus, we are confident that our RR Lyrae star sample will consist predominantly of halo objects. Of course, kinematic information is required to be certain of population membership. Finally, an OoII component may extend to smaller amplitudes than an OoI component. The amplitude cut should optimally be extended to smaller amplitudes at longer periods, but our detection efficiency below 0.3 magnitudes is relatively low at the faint end. While this cut may preferentially remove OoII RR Lyrae stars, the LONEOS - I dataset cannot efficiently probe this region period-amplitude space.

Using our visual classifications (i.e., “good”, “fair”, and “bad”), we determined the thresholds for two additional cuts: uniformity and smoothness. These cuts were performed simultaneously, and their thresholds were set to minimize the number of “bad” objects and maximize the number of “good” objects. First, we required that the light curves have a degree of uniformity. The phased data points should be distributed from zero to one as randomly and uniformly as possible. In order to measure this, we divided the phased light curve into 10 equally spaced bins, and binned the data points. We required that at least 7 bins have at least one measurement. Thus, at most 30% of the phase is allowed to contain no data points. We referred to this as the “N gap” test. Secondly, we examined the goodness of fit of the RR Lyrae star template relative to the fit to a constant magnitude. We define this statistic as: $\Delta\chi^2 = (\chi_{constant}^2 - \chi_{RR}^2)/\chi_{RR}^2$,

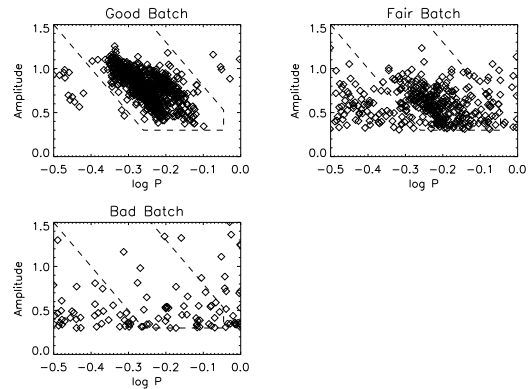


FIG. 6.— These three period-amplitude distributions show the objects which were successfully fit to an RR Lyrae template light curve. The plots show the amplitude (in LONEOS - I instrumental magnitudes) versus the logarithm of the period measured in days. They have been manually classified into three categories, “good”, “fair”, “bad”. The “good” and “fair” distributions are consistent with being RR Lyrae with some scatter, while the “bad” category is randomly distributed. The dashed lines indicates the region of period-amplitude space where RR Lyrae stars are expected to lie. This region is large enough to encompass a wide range of metallicities and Oosterhoff types.

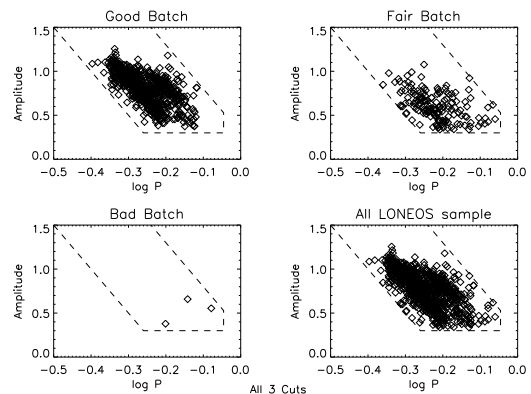


FIG. 7.— We show the resulting objects after we have applied the period-amplitude cut and two additional light curve quality cuts described in the text. The lower-right panel shows the final RR Lyrae sample.

where we use a reduced χ^2 for all the fits. This statistic measures the scatter about the six RR_{ab} templates, and thus smoothness of the period-folded data. For this sample, we used $\Delta\chi^2 > 5$.

Together, these three cuts reject 8%, 60%, 97% from the “good”, “fair”, and “bad” samples, respectively. Figures 6 and 7 show the results of the final three cuts. The sample presented in this paper are restricted to mean magnitudes ranging from 13.0 to 17.5. We will discuss the completeness of this sample in the following sections. We also removed known RR Lyrae that are members of globular clusters and RR Lyrae within the tidal radius of the globular clusters in our survey volume, a total of 19 objects. Our final sample consists of 838 ab -type RR Lyrae, which are solely based on temporal photometric data. Table 1 lists the properties of this sample. Two sample light curves are shown in Figure 8. To date, this represents the largest single sample of period-folded RR Lyrae stars in the stellar halo.

As a simple test of the contamination of our RR Lyrae sample, we explored the colors of a subset of these ob-

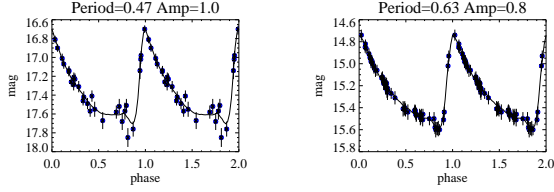


FIG. 8.— Two examples of phased RR Lyrae light curves. The lightcurves are shown over two full phases.

TABLE 1
PROPERTIES OF 838 LONEOS - I RR LYRAE SAMPLE

| RA | DEC | $\langle M_{LONEOS\ V} \rangle$ | Period | Amplitude |
|------------|------------|---------------------------------|----------|-----------|
| 231.923019 | -22.413485 | 14.48 | 0.606328 | 0.890 |
| 234.829575 | -22.006363 | 16.45 | 0.644697 | 0.734 |
| 303.111725 | -23.159113 | 15.18 | 0.608629 | 0.812 |
| 302.516479 | -22.789234 | 15.62 | 0.670238 | 0.705 |
| ⋮ | ⋮ | ⋮ | ⋮ | ⋮ |
| 259.791656 | 45.140347 | 15.25 | 0.468290 | 1.083 |

NOTE. — This table list a few properties of the 838 LONEOS - I RR Lyrae sample. The coordinates (RA,DEC) are given in decimal degrees in the epoch of J2000.0. The mean magnitudes ($\langle M_{LONEOS\ V} \rangle$) are tied to the V_{SDSS} system. The periods are given in days. Finally, the amplitudes are measured from minimum to maximum brightness as defined by the RR Lyrae template that best fit the lightcurve. [The complete version of this table is in the electronic edition of the Journal. The printed edition contains only a sample.]

jects. RR Lyrae should be identifiable on the basis of Sloan Digital Sky Survey (SDSS) photometry alone (Krisciunas 2001; Krisciunas et al. 1998). 78 of the LONEOS - I RR Lyrae have clean SDSS Data Release 3 photometry (Abazajian et al. 2005). Figure 9 shows the color-color diagrams constructed from SDSS DR3 photometry. RR Lyrae stars are contained in a small region of SDSS color-color space (Ivezić et al. 2005) as shown by the rectangular areas outlined in the figure. The contours indicate the location of the stellar locus in each of the 2D slices through the SDSS color-color space. The red points are LONEOS - I RR Lyrae stars (78) with SDSS DR3 photometry. There are only two objects which do not pass the $g-r$ cut, but are consistent with RR Lyrae stars in the three other colors. Thus, virtually all of these objects have colors consistent with RR Lyrae stars. We conclude that our RR Lyrae sample has a low degree of contamination.

The survey contains fields with Galactic latitude as low as 10 degrees. Thus, there is a possibility that RR Lyrae from the thick disk have contaminated our sample. Our period-amplitude cut likely has removed most of the thick disk RR Lyrae, but let us investigate how much thick disk contamination our sample might have using Galactic models. We use a double exponential to model the thick disk with a scale height of 0.7 kpc and scale length of 3.0 kpc (Layden 1995). These scales are based on measurements using RR Lyrae stars. Our halo is modeled as a power law with an index of -2.43 , which is the value we found using the LONEOS - I RR Lyrae (See the next section for details). We assume that the thick disk is 10 times more populous than the stellar halo in the Solar Neighborhood, and the measured stellar number density is $0.1pc^{-3}$ (Reid & Hawley 2000). We also assume that the frequencies of RR Lyrae stars in the

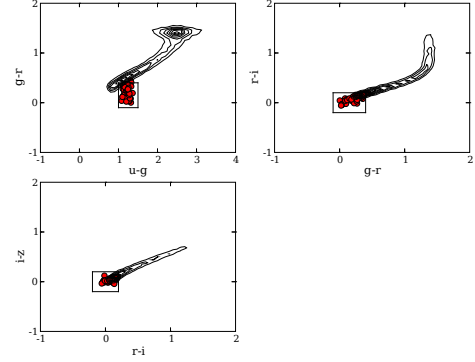


FIG. 9.— These color-color diagrams are constructed from SDSS photometry. The contours indicate the location of the stellar locus in each of the 2D slices through the SDSS color-color space. The rectangular areas are the RR Lyrae color boundaries are from Ivezić et al. (2005). The red points are LONEOS - I RR Lyrae (78) with SDSS DR3 photometry. There are only two objects which do not pass the $g-r$ cut, but are consistent with RR Lyrae stars in the three other colors. Thus, virtually all of these objects have colors consistent with RR Lyrae stars.

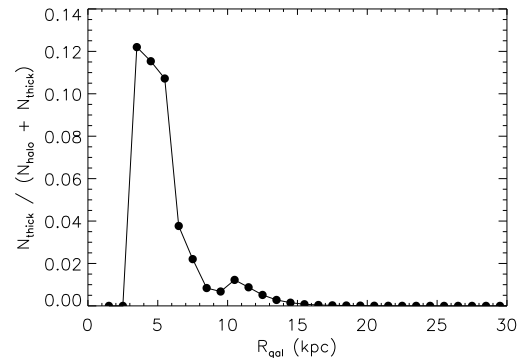


FIG. 10.— This figure shows the predicted fraction of thick disk stars relative to halo stars which is expected in the LONEOS - I survey volume as a function of Galactocentric Radius.

thick disk and halo are identical. This is a conservative assumption since thick disk RR Lyrae stars frequencies will be suppressed since thick disk RR Lyrae stars are more metal-rich. Given these parameters, we calculate the anticipated fraction of thick disk stars relative to halo stars in the LONEOS - I survey volume. Figure 10 shows this fraction as a function of Galactocentric Radius. This figure shows that the fraction of thick disk stars to halo stars is about 12% even at the smallest radii, where the largest contamination is expected. This low fraction of thick disk stars and our period-amplitude cut give us confidence that the contamination of thick disk stars in our sample is negligible.

In order to investigate how well we recover various RR Lyrae light curve parameters, we simulated RR Lyrae light curves with known parameters and examined the recovered parameters using the RR Lyrae period and light curve fitting procedure described above. We used the actual cadence for each subfield to generate simulated time series of RR Lyrae stars using template RR Lyrae light curves from Layden (1998) with various mean magnitudes. We used a known RR Lyrae period-amplitude distribution (Smith 1995) to generate the simulated time

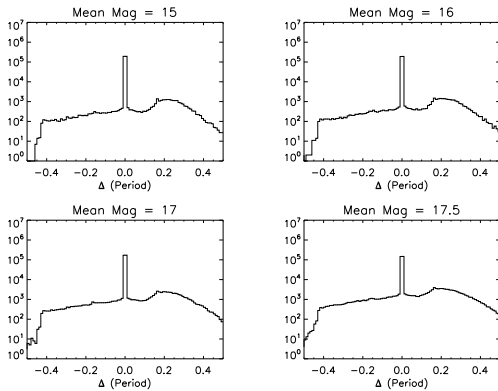


FIG. 11.— We have simulated RR Lyrae light curves with a range of periods and examined the periods recovered using our phasing and light curving fitting described in Section 3.1. The histograms show the difference between the input and recovered periods for four mean magnitudes. The fraction contained within ± 0.01 days are: 0.92, 0.90, 0.81, 0.70, for mean magnitudes of 15, 16, 17, and 17.5, respectively.

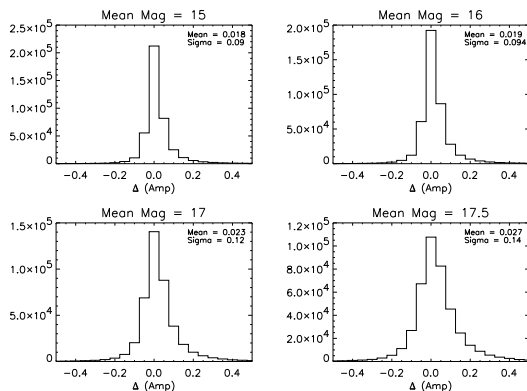


FIG. 12.— These histograms show the the residual between the input and recovered amplitudes from simulated RR Lyrae light curves of various mean magnitudes. The residual increases with mean magnitude. In addition, the distributions are skewed; the recovered amplitudes tend to be underestimated.

series with random phase. We assigned photometric error bars and smear the simulated light curves based on the magnitude dependence of the LONEOS - I photometric errors. In Figure 11, the residuals of the input and recovered periods are shown. Periods are recovered with good accuracy. The fraction of simulated RR Lyrae contained within ± 0.01 days are: 0.92, 0.90, 0.81, 0.70, for mean magnitudes of 15, 16, 17, and 17.5, respectively. We will investigate the possibility of misidentified periods in the next section when we discuss the Oosterhoff components.

Similarly, Figure 12 shows the residuals of the input and the recovered amplitude. The residual increases with mean magnitude. In addition, the distributions are skewed; the recovered amplitudes tend to be underestimated. This is a consequence of the asymmetric shape of *ab*-type RR Lyrae light curves, and the sparseness of our sampling. However, we find that the underestimation of amplitudes does not depend on the input period. Thus, underestimating the amplitude will only have the effect of shifting RR Lyrae stars downward in a period-amplitude diagram. We will discuss this more in the next section.

3.2. Completeness

In this section, we estimate our efficiency in detecting RR Lyrae stars (i.e., the completeness of the sample). The completeness depends on a number of RR Lyrae parameters, but most strongly on their magnitude and amplitude. One of our scientific goals is to measure the number density of RR Lyrae stars as a function of position in the Galaxy. This requires that we estimate the detection efficiency as a function of Galactic position.

We divided our completeness analysis into photometric and temporal parts. In order to estimate the photometric efficiency, we take a clean, unblended, and dereddened sample of stellar objects from SDSS DR3, which are contained in the LONEOS - I footprint. Since the SDSS detection limits are at least 2 magnitudes deeper than LONEOS, we can use SDSS to understand the degree to which LONEOS - I is photometrically complete. Using this sample, we performed a proximity query using our LONEOS - I database. For each SDSS star, we search in the LONEOS - I database for objects within 1.8 arcsecs. A total of 58,591 SDSS stars are queried in the LONEOS - I database. Next, we count the number of detections and non-detections of the object in every LONEOS - I image. A measurement is considered a non-detection if any one of the following criteria are true:

- Signal-to-noise ratio is below threshold (5σ)
- Measurements are flagged by photometric pipeline as bad (e.g., blended, pixel defects, non-stellar shape, cosmic ray hit)
- More than one LONEOS - I object is detected, which indicates problems with time series generation.

These criteria are also used for the later analysis.

Thus, this comparison with SDSS not only gives us an estimate of the photometric completeness based on signal-to-noise, but also an estimate of the efficiency of the photometric pipeline. The last two non-detection criteria are generally independent of magnitude. Thus, these will contribute to an overall reduction across all magnitudes. This is why the efficiency converges to only $\sim 90\%$ in the bright magnitude range. Figure 13 shows the LONEOS - I photometric completeness. We use the following parameterization for photometric efficiency shown in Figure 13:

$$f(V_{SDSS}) = \frac{1}{1 + e^{\frac{V_{SDSS} - 18.74}{0.47}}} - 0.11. \quad (19)$$

In addition, we did not find a significant dependence on the photometric completeness curves with position on the sky. Thus, we use this as our universal photometric completeness function.

Using this parameterized photometric completeness, we performed the temporal completeness analysis. We generated simulated RR Lyrae times series in the same manner as described in Section 3.1, except that we incorporated the parameterized photometric completeness, which provided a detection probability as function of magnitude. We randomly rejected individual time series measurements based on this detection probability. Given the large number of subfields ($\sim 15,000$), we performed this analysis on one “typical” subfield per field,

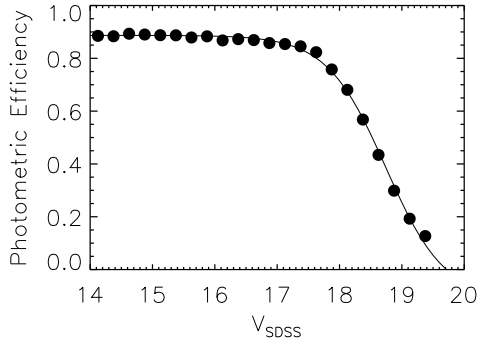


FIG. 13.— We have taken a clean sample of unblended SDSS DR3 stars and queried the LONEOS - I database for a detection in each image in the database. This figure shows the overall photometric completeness (image-by-image) assuming SDSS is complete. Note that non-detection also include measurements that were flagged as being problematic.

which had the median number of images; the number of images for subfields in a given field does not vary much. Thus, we perform this analysis on 421 “typical” subfields. We generated 1000 simulated time series for each “typical” subfield and for each magnitude. All the simulated RR Lyrae times series were analyzed using the same selection criteria (see Figure 4) as those used to generate the real LONEOS - I RR Lyrae catalog. The completeness functions were generated based on the percentage of simulated time series which passed our RR Lyrae selection criteria. The completeness functions as a function of magnitude (M) for the “typical” subfields were parametrized by the following function:

$$f'(M_{LONEOS\ V}) = \frac{1}{1 + e^{\frac{M_{LONEOS\ V} - \mu}{T}}} - Z, \quad (20)$$

where μ is the characteristic magnitude cutoff, T is the width of the cutoff, and Z is a horizontal offset. Figure 14 shows the detection efficiency as a function of magnitude for four fields. All magnitudes have been corrected for Galactic extinction using Schlegel et al. (1998). These efficiencies are used when we calculate the survey volume and corrected RR Lyrae star number densities in the following section. The completeness function for the “typical” subfield is used for all subfields of the same field. A histogram of the number of images in the “typical” subfields is shown in the top left plot of Figure 15. The median number of images is 31. In order to give a sense of the dependence of the completeness on the number of images, Figure 15 shows the correlations of the magnitudes at 50% completeness and the completeness at the bright end ($1-Z$ in Equation 20) with the number of images in the top right and bottom left plots, respectively. The completeness is generally correlated with the number of images.

4. ANALYSIS

In this section, we explore the bulk properties of the LONEOS - I RR Lyrae star sample that was described in the previous section. First, we present the spatial distribution of the entire sample. Next, we present the period-amplitude distribution of the sample. Finally, we explore the spatial distributions of the different populations that emerge from the period-amplitude distribution.

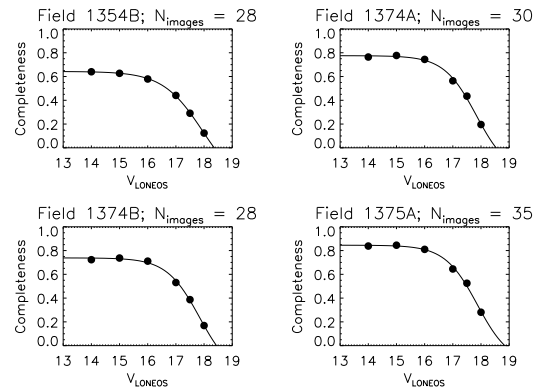


FIG. 14.— The RR Lyrae star completeness (photometric and temporal) for four fields with different number of images are shown. Note that even though fields 1354B and 1374B have identical numbers of images, the completeness curves are different. This is caused by the different cadences of these two fields. These curves are used to correct the effective volume in the density measurements.

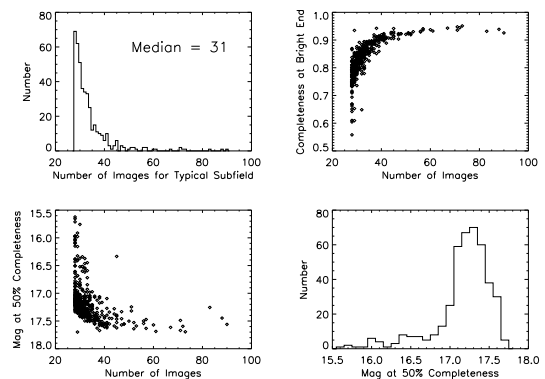


FIG. 15.— This figure shows various parameters and correlations related to the RR Lyrae star completeness (photometric and temporal). First, the top left plot is a histogram of the number of images for the typical subfields. The median number of images is 31. The top right scatter plot shows the dependence of the magnitude at the bright end ($1-Z$ in Equation 20) on the number of images. This gives a sense of the completeness for bright stars, where signal-to-noise ratio is high. On the other hand, the bottom left scatter plot shows the dependence of the magnitude at 50% completeness on the number of images, which gives a sense of the completeness towards the faint end. Finally, the bottom right histogram shows the distribution of the magnitude at 50% completeness.

4.1. Radial Density Distribution

As described in previous sections, we tie our absolute photometry to synthetic SDSS-based magnitudes (V_{SDSS}), $M_{LONEOS\ V}$. This allows for a straightforward calculation of distances from the intensity-weighted mean magnitudes. Distances are calculated from the following formula:

$$d = 10^{\frac{\langle M_{LONEOS\ V} \rangle - M_V - 10}{5}} \text{ kpc}, \quad (21)$$

We will use RR Lyrae absolute magnitudes of $M_V = +0.71 \pm 0.12$ (Layden et al. 1996) derived from statistical parallax analysis for a sample with $\langle [Fe/H] \rangle = -1.61$. Assuming that the Sun is at -7.8 kpc (Carney et al. 1995) from the galactic center along the y -axis ($x_{gal}, y_{gal}, z_{gal} = (0, -7.8, 0)$ kpc), we calculate the galactocentric 3-D coordinates of each RR Lyrae star.

We measure the spherically symmetric radial density

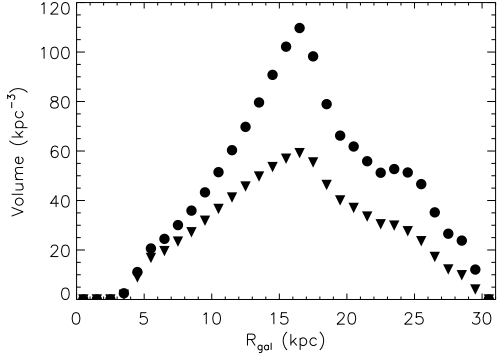


FIG. 16.— This figure shows the raw (circles) and the detection efficiency-corrected (triangles) survey volumes. Note that the difference between the two curves is not monotonically increasing because there are lines-of-sight which are pointed towards the Galactic Center and also the anti-Center which contribute at different ranges of Galactocentric radius. If the volume calculation assumes that the Sun is at the center of the Galaxy, the difference between these two curves does indeed increase monotonically.

distribution by counting the number of RR Lyrae stars in galactocentric radial bins and calculating the survey volume contained in each bin. We use 1 kpc bins for all the density distributions. This provides us with a measure of the radial density distribution averaged along the survey lines-of-sight. Using the boundaries of the survey we numerically integrate the volume contained in each radial bin, taking into account detection efficiency at each position in the Monte Carlo integration. Figure 16 shows the survey effective volume distribution.

Assuming a spherically symmetric distribution, Figure 17 shows the radial profile for our sample with mean magnitudes in the range [13,17.5] with $M_V = +0.71$. The one-sigma, asymmetric Poisson error bars are assigned and calculated using the method of Gehrels (1986). Using non-linear least squares, we fit power laws to the radial density distributions:

$$\rho(R_{gal}) = (397 \pm 56) \times R_{gal}^{(-2.43 \pm 0.06)} \text{ (kpc}^{-3}\text{)}. \quad (22)$$

with χ^2 per degree of freedom of 0.91. All fitted parameter estimates are calculated using a Monte Carlo bootstrap technique (Press et al. 1992). Table 2 summarizes results from other surveys. This result is within $1 - \sigma$ of the QUEST-I (Vivas & Zinn (2006), $M_V = +0.55$, $R_{SUN} = 8.0$ kpc) and the SDSS (Ivezić et al. (2000), $M_V = +0.7$, $R_{SUN} = 8.0$ kpc) results, assuming a spherical halo distribution. The power law exponent is slightly sensitive to the distance to the Galactic Center. If $R_{SUN} = 8.5$ kpc, then exponent is reduced to -2.50 ± 0.05 . As shown in Table 2, the measured distance to the Galactic Center has been decreasing with time. This means that earlier measurements will tend to have steeper profiles than our measurement.

The shapes of the stellar and dark matter halos should have encoded in them some information of their formation process. In general, the isodensity contours for the RR Lyrae number density can be described by an ellipsoid:

$$\frac{x^2}{a^2} + \frac{y^2}{b^2} + \frac{z^2}{c^2} = 1. \quad (23)$$

Let us consider the case where $a = b$ (i.e., a spheroid)

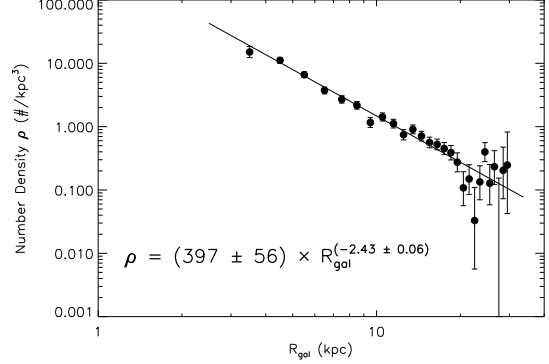


FIG. 17.— The radial density distribution of 838 *ab*-type RR Lyrae with a mean magnitude range from 13.0 to 17.5, using $M_V = +0.71$. We do not find any statistically significant deviations from a smooth stellar halo. Our survey volume does not intersect known locations of the tidal debris from the Sagittarius dwarf galaxy.

and define the flattening ratio as, $q \equiv c/a$. Thus, the isodensity contours can be described as:

$$x^2 + y^2 + \frac{z^2}{q^2} = a^2, \quad (24)$$

where $q < 1$ and $q > 1$ are oblate and prolate spheroids, respectively. It is widely observed that the inner regions ($R_{gal} = 5 - 10$ kpc) of the stellar halo are highly flattened ($q \sim 0.5$), while the outer regions are more spherically symmetric (e.g., Kinman et al. 1966; Preston et al. 1991; Chiba & Beers 2000). We fit spheroids with various constant flattening to the LONEOS - I RR Lyrae. In addition, we also use a model with a spatial variable flattening ratio (Preston et al. 1991), where q varies as function of semi-major axis, a :

$$q = \begin{cases} q_0 + [1 - q_0] \frac{a}{20} & \text{if } a < 20 \text{ kpc} \\ 1 & \text{if } a > 20 \text{ kpc} \end{cases}$$

where $q_0 = 0.5$ and a is the semi-major axis. In this variable q model, the flattening smoothly varies from 0.5 to 1.0 over the course of 20 kpc. Figure 18 shows the radial profiles and power law fits for both the spherical and the variable flattening models. The power law exponents, χ^2 , degrees of freedom, and χ^2 probabilities are listed in Table 3. The degrees of freedom are not constant since the data are binned and the value of a depends on q . All the flattening models have larger χ^2 probability than the spherically symmetric model indicating that flattened models are favored, but there is no clear minimum in the χ^2 probabilities. The variable q model yields a steeper density profile with a power law exponent of -3.15 ± 0.07 with a χ^2 per degree of freedom of 0.7. This agrees with most other RR Lyrae surveys (Table 2).

The poor constraint on the stellar halo flattening from the LONEOS - I RR Lyrae is likely a result of the fact that the Galactic latitude distribution of these RR Lyrae are highly concentrated at mid-range Galactic latitude with no fields near the Galactic Poles. The difference between the spherical and flattened model is smallest at lower Galactic latitudes.

All the recent RR Lyrae surveys are in disagreement with Chiba & Beers (2000) who used ~ 1200 non-kinematically selected metal poor stars. One reason for

TABLE 2
 HALO RR LYRAE SURVEY COMPARISONS

| Survey | Tracer | Exponent | Flattening Ratio (q) | Objects | R_0 (kpc) | Comment |
|-------------------------------|--|------------------|--------------------------------|---------|-------------|---|
| LONEOS - I (All) | RR Lyrae | -2.43 ± 0.06 | $q = 1$ | 838 | 7.6 | $M_V = +0.71$ |
| LONEOS - I (All) | RR Lyrae | -3.15 ± 0.07 | Variable q | 838 | 7.6 | $M_V = +0.71$ |
| LONEOS - I (Oo I) | RR Lyrae | -2.26 ± 0.07 | $q = 1$ | 619 | 7.6 | $M_V = +0.71$ |
| LONEOS - I (Oo II) | RR Lyrae | -2.88 ± 0.11 | $q = 1$ | 219 | 7.6 | $M_V = +0.71$ |
| QUEST-I (Vivas & Zinn (2006)) | RR Lyrae | -2.5 ± 0.1 | $q = 1$ | 395 | 8.0 | $M_V = +0.55$ |
| QUEST-I (Vivas & Zinn (2006)) | RR Lyrae | -3.1 ± 0.1 | Variable q | 395 | 8.0 | $M_V = +0.55$ |
| SDSS (Ivezic et al. (2000)) | RR Lyrae | -2.7 ± 0.2 | $q = 1$ | 148 | 8.0 | $M_V = +0.7$ |
| Chiba & Beers (2000) | Halo ($\langle [Fe/H] \rangle \leq -1.8$) | -3.55 ± 0.13 | Variable q ($q_0 \sim 0.65$) | 413 | ... | Kinematics |
| Chiba & Beers (2000) | Halo ($-1.6 < \langle [Fe/H] \rangle \leq -1.0$) | -3.47 ± 0.18 | Variable q ($q_0 \sim 0.55$) | 331 | ... | Kinematics |
| Wetters & McGraw (1996) | RR Lyrae | -3.0 ± 0.08 | $q = 1$ | 42 | 7.6 | $M_V = +0.74$ |
| Wetters & McGraw (1996) | RR Lyrae | -3.5 ± 0.08 | Variable q | 42 | 7.6 | $M_V = +0.74$ |
| Preston et al. (1991) | RR Lyrae | -3.2 ± 0.1 | Variable q | 47 | 8.0 | $M_V = +0.6$ |
| Saha (1985) | RR Lyrae | -3.0 | $q = 1$ | 29 | 8.7 | P-L-A relation ($M_B = M_{bol} + 0.34$) |
| Zinn (1985) | Globular Clusters | -3.5 | ... | 121 | ... | ... |
| Hawkins (1984) | RR Lyrae | -3.1 ± 0.2 | $q < 0.9$ | 24 | 8.7 | $M_B = +0.9$ |
| Oort & Plaut (1975) | RR Lyrae | -3.0 | $q < 0.8$ | 1108 | 8.7 | $M_B = +0.9$ |
| Kinman et al. (1966) | RR Lyrae | -3.5 | $q = 0.6 - 0.8$ | 38 | 10.0 | $M_V = +0.42$ |

NOTE. — We compare the LONEOS - I RR Lyrae survey results to those of other surveys using RR Lyrae stars and other tracers.

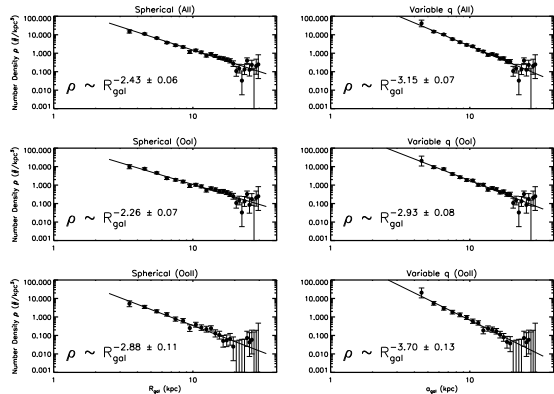


FIG. 18. — Radial density profiles for spherical and variable flattening models are shown in the left and right columns, respectively. The variable flattening model is that of Preston et al. (1991), where the flattening ratio variable from 0.5 to 1.0 with increasing distance from the Galactic Center. The top row of plots are for the entire sample of RR Lyrae stars. The second and third rows are for sub-samples of RR Lyrae, classified as Oosterhoff I and II, respectively. The LONEOS - I RR Lyrae data are fit by the spherical and variable flattening models equally well. The fits are not statistically different.

the difference could be the method used. RR Lyrae surveys use 3D Galactocentric coordinates to measure densities. In these surveys, the completeness and survey volume are relatively well-defined. However, Chiba & Beers (2000) use data derived from many different surveys and is not a volume-limited sample. They use a maximum likelihood method which relies on kinematic information and Jeans' theorem to measure the power law. Since the completeness and survey volumes are not easily understood, it is not possible to measure the density distribution using a binning technique. Thus, it is difficult to understand if there is a real difference between RR Lyrae stars and generic metal-poor stars. In addition, RR Lyrae stars and the metal poor halo stars from Chiba & Beers (2000) may possibly be tracing different populations. RR Lyrae abundances are influenced by the horizontal branch morphology of the RR Lyrae progenitor system. Thus, they may not reveal the entire history of Galactic formation and could have different spatial distributions than a sample of metal poor halo stars.

4.2. Period-Amplitude Distribution

The period-amplitude distribution of RR Lyrae stars can be used to explore the formation history of the Galac-

 TABLE 3
 FLATTENING FITS

| Sample | Flattening Ratio (q) | Exponent | χ^2 | Degrees of Freedom (ν) | Probability ($Q(\chi^2, \nu)$) |
|--------|----------------------|----------|----------|------------------------------|----------------------------------|
| All | 1.0 | -2.43 | 24.7 | 24 | 0.42 |
| All | Variable q | -3.15 | 18.3 | 23 | 0.74 |
| All | 0.9 | -2.48 | 16.1 | 24 | 0.88 |
| All | 0.8 | -2.53 | 17.7 | 24 | 0.82 |
| All | 0.7 | -2.57 | 14.4 | 23 | 0.91 |
| All | 0.6 | -2.58 | 19.8 | 23 | 0.65 |
| All | 0.5 | -2.57 | 13.4 | 22 | 0.92 |
| All | 0.4 | -2.57 | 15.4 | 22 | 0.84 |
| All | 1.1 | -2.35 | 17.5 | 25 | 0.86 |
| All | 1.2 | -2.29 | 19.1 | 25 | 0.79 |
| OoI | 1.0 | -2.26 | 18.9 | 24 | 0.76 |
| OoI | Variable q | -2.93 | 16.0 | 23 | 0.86 |
| OoI | 0.9 | -2.29 | 13.8 | 24 | 0.95 |
| OoI | 0.8 | -2.36 | 14.8 | 24 | 0.93 |
| OoI | 0.7 | -2.40 | 12.6 | 23 | 0.96 |
| OoI | 0.6 | -2.42 | 19.8 | 23 | 0.65 |
| OoI | 0.5 | -2.41 | 10.5 | 22 | 0.98 |
| OoI | 0.4 | -2.41 | 10.9 | 22 | 0.98 |
| OoI | 1.1 | -2.18 | 13.3 | 25 | 0.97 |
| OoI | 1.2 | -2.15 | 15.9 | 25 | 0.92 |
| OoII | 1.0 | -2.88 | 7.2 | 24 | 0.9996 |
| OoII | Variable q | -3.70 | 5.9 | 23 | 0.9998 |
| OoII | 0.9 | -2.97 | 5.6 | 24 | 0.9999 |
| OoII | 0.8 | -3.02 | 5.7 | 24 | 0.9999 |
| OoII | 0.7 | -3.09 | 7.5 | 23 | 0.9990 |
| OoII | 0.6 | -3.07 | 5.8 | 23 | 0.9998 |
| OoII | 0.5 | -3.01 | 9.6 | 22 | 0.9895 |
| OoII | 0.4 | -3.04 | 13.0 | 22 | 0.9331 |
| OoII | 1.1 | -2.80 | 10.0 | 25 | 0.9966 |
| OoII | 1.2 | -2.71 | 11.8 | 25 | 0.9881 |

NOTE. — Power law fits with varying flattening models.

tic halo (e.g., Catelan 2006). If some fraction or all of the stellar halo was formed from the accretion of dwarf galaxies, which might have very diverse chemical histories and ages (i.e., different horizontal branch morphologies), the signatures of these accretion events should be imprinted in the period-amplitude distribution. Thus, accretion activity can be probed even after phase-space has been sufficiently mixed that spatial coherence is lost.

Our large sample of RR Lyrae stars allows us to further investigate this possibility and to explore differences in the two components. In lower-right panel of Figure 7, we plot the period-amplitude distribution of 838 ab-type RR Lyrae stars. Since LONEOS uses an unfiltered CCD system, whose sensitivity peaks in the red, amplitudes for our RR Lyrae will be systematically smaller than those taken in the V-band. The observed amplitude of RR Lyrae increases as you observe them in bluer passbands.¹ Using a subset of LONEOS - I RR Lyrae

¹ Note that the transformation to the V_{SDSS} magnitude system does not affect the measured LONEOS - I amplitudes. The amplitudes are strictly a function of the passband used.

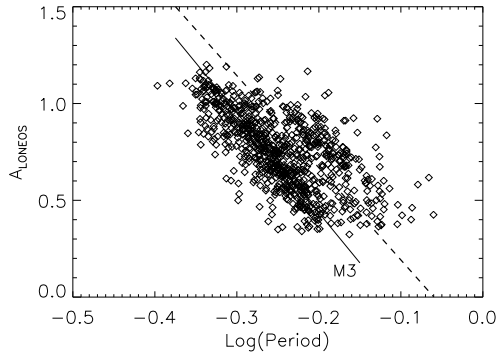


FIG. 19.— The LONEOS RR Lyrae period-amplitude distribution (same as Figure 7) with the linear log(period)-amplitude relation for globular cluster M3 (OoI) superimposed (solid line). Note the amplitudes are based on the unfiltered response of the LONEOS - I camera system. The M3 relation has been converted to the LONEOS - I amplitude scale. We derived a conversion between LONEOS - I amplitude and V-band amplitudes from Cacciari et al. (2005). The dashed line indicates where we divide our sample into OoI and OoII components.

(12 stars) which have previously measured V-band amplitudes taken from SIMBAD database, we have empirically derived a scaling relation between the LONEOS amplitudes (A_{LONEOS}) and V-band amplitudes (A^V) and scaled the M3 RR Lyrae period-amplitude relation to the LONEOS - I amplitude scale. The mean value of A_{LONEOS}/A^V is 0.7 with a standard deviation of 0.1. Figure 19 shows that data from the lower-right panel in Figure 7 overlaid with the linear period-amplitude relation for M3 (the quintessential OoI globular cluster) (Cacciari et al. 2005) corrected to the LONEOS - I amplitude scale. Despite only having 12 stars to scale LONEOS amplitudes to V-band amplitudes, the main locus agrees well with the period-amplitude relation of M3. Thus, we associate the main locus with the OoI component of the stellar halo. In addition, Figure 19 shows a striking concentration of RR Lyrae (26% of the total sample) with longer periods offset from the main locus of points.

We fit a line to the primary locus ($P_{primary}(A)$) and measure the period shift,

$$\Delta \text{Log}(\text{Period}) = P_{RR}(A) - P_{primary}(A), \quad (25)$$

which refers to the Log(Period) distance (at fixed amplitude) of *each* RR Lyra ($P_{RR}(A)$) from this best fit line ($A = -4.76 \times \text{Log}(P_{primary}) - 0.51$). Figure 20 shows the distribution of the period shift at fixed amplitude from the main locus. This figure clearly shows the existence of a secondary locus. It is shifted from the main locus by $\Delta \text{Log}(P) \sim 0.075^2$, which is approximately the shift between RR Lyrae in OoI to OoII globular clusters (e.g., Sandage et al. 1981; Clement & Shelton 1999). Thus, we associate the main locus of points with an OoI halo component, and the shifted locus with an OoII halo component.

In Figure 21, we plot the period shift distribution of 395 RR Lyrae from the QUEST-I catalog (Vivas et al. 2004) with mean magnitudes in the range [13.5, 19.7] as well as the LONEOS-I period-shift distribution. This QUEST-I distribution also contains a sizable fraction

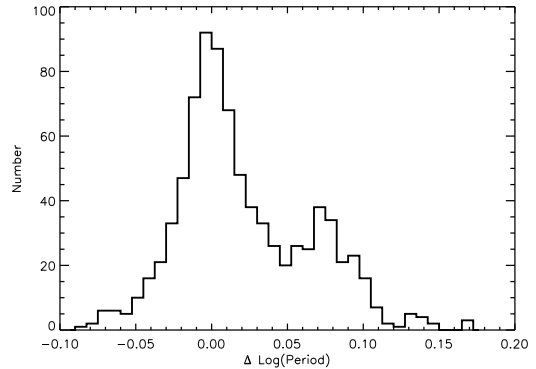


FIG. 20.— Histogram of the period shift of RR Lyrae relative to the primary locus (OoI). We fit a line to the primary locus and measure $\Delta \text{Log}(\text{Period})$ which refers to the Log(Period) distance (at fixed amplitude) of *each* RR Lyrae star from this best fit line. Thus, the primary locus is centered at $\Delta \text{Log}(\text{Period}) = 0.0$. The location of the secondary locus is located at approximately the location where we would expect the OoII locus (Sandage et al. 1981; Cacciari et al. 2005). For the subsequent analysis, we divide our sample at $\Delta \text{Log}(\text{Period}) = 0.045$, where period is measured in days.

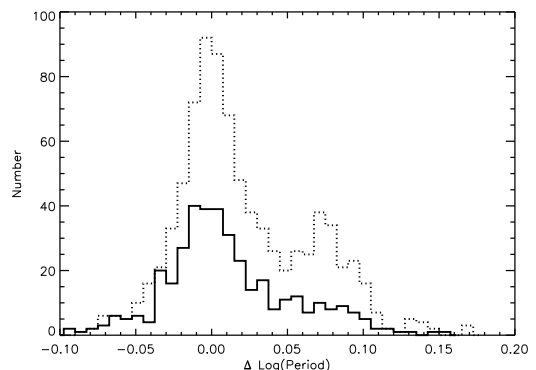


FIG. 21.— Period shifts (with respect to M3) of the QUEST-I RR Lyrae Survey is shown as a solid line, while the LONEOS-I period shifts are shown as a dashed line. In contrast to the LONEOS-I sample, there is no clearly displaced secondary peak associated with an OoII component for the QUEST-I sample. However, there is a long period tail.

($\sim 20\%$) of longer period RR Lyrae than the main OoI locus. Catelan (2006) has pointed out that the Oosterhoff classification the QUEST-I RR Lyrae may be unreliable due to their sparse temporal sampling. This could cause a smearing of the period shift distribution in the QUEST-I data.

It has been well established that OoI and OoII globular clusters show spatial and kinematic differences, which may signify different origins (Lee & Carney 1999). It is natural to ask if the OoI and OoII components of the stellar halo show similar differences. We divided our sample into the two components described above. The division was positioned at the minimum of the period shift distribution, $\Delta(P) = 0.045$. The division is denoted by the dashed line in Figure 19. The radial number density profiles for each component are shown in Figure 22. From these profiles, we derive the following radial dependences:

$$\rho_{OoI} \sim R^{-2.26 \pm 0.07}, \quad (26)$$

² Periods are measured in days.

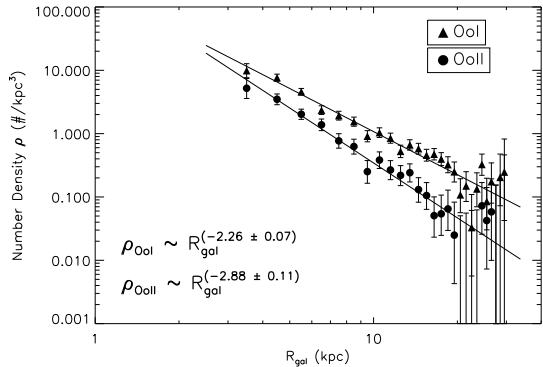


FIG. 22.— The spherically symmetric ($q=1$) radial distribution for the OoI and OoII components. The bins with zero density are included in the fit; the 1σ Poisson upper limits are calculated using the method of Gehrels (1986).

$$\rho_{OoII} \sim R^{-2.88 \pm 0.11}. \quad (27)$$

The OoII component has a steeper profile than the OoI component. This is consistent with Lee & Carney (1999) who, using a smaller RR Lyrae sample, found that the OoI component dominated farther from the Galactic plane, possibly indicating that the OoII component falls off more rapidly than the OoI component. In the following sections, we will examine whether this difference could be caused by some systematic effect in the detection of the two populations.

The possibility of an intermediate Oosterhoff halo component still exists, but our current sample cannot address this. It is critical to effectively identify and veto RR Lyrae which exhibit the Blazhko effect (i.e. amplitude and phase variations). These stars will add scatter to the period-amplitude relation (Cacciari et al. 2005). In addition, we have found that the LONEOS - I measured RR Lyrae amplitudes tend to be underestimated (Figure 12). This effect would tend to diminish the number of RR Lyrae with intermediate Oo classification.

Additionally, microlensing surveys (e.g., MACHO, OGLE) have found that as much as a third of RR Lyrae stars in the LMC and SMC exhibit the Blazhko effect (e.g., Alcock et al. 2000). In order to address the possibilities of an intermediate Oo component, we need better temporal coverage (e.g., Catelan 2006). A mixture of OoI and OoII could masquerade as an intermediate.

Is the difference in radial distributions associated with the Oosterhoff effect? Does the Oosterhoff effect manifest itself in such a way? Previously, we have chosen to divide our full sample into two components that resemble OoI and OoII populations; this maximizes the role of the Oosterhoff effect on the sample. Instead, we now divide our entire sample along a line in period-amplitude space perpendicular to the Oosterhoff dividing line, minimizing the role of the Oosterhoff effect. The resulting power law exponents (α) are consistent with each other ($\alpha = -2.50 \pm 0.07$ and $\alpha = -2.39 \pm 0.1$). This indicates that the Oosterhoff effect is likely associated with differing radial distributions.

5. DISCUSSION

As described in the previous section, the LONEOS - I RR Lyrae data have two interesting characteristics. The

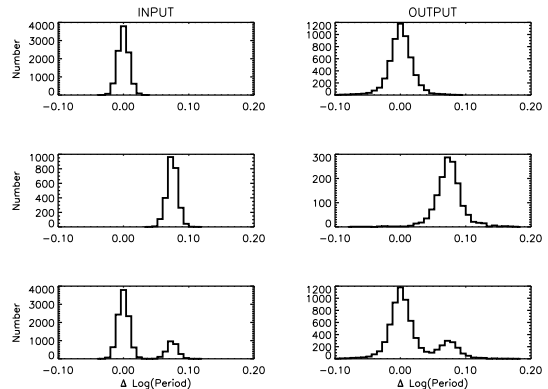


FIG. 23.— We simulated RR Lyrae light curves with period and amplitude distributions of OoI and OoII RR Lyrae stars. These simulated RR Lyrae light curves were processed through our detection pipeline. This figure shows the period shift histograms for one field with 28 images (1374B). We have scaled the OoII input sample to contain 26% of the OoI component, which is what we observe in the LONEOS - I sample. The detection process tends to broaden the period shift distributions and produces long tails. However, the OoI and OoII are still recognizable after the detection process.

Oosterhoff effect is manifest in the Galactic stellar halo. Moreover, the two Oosterhoff components we have identified have distinct radial distributions.

5.1. Potential Systematic Errors and Biases

In order to test whether the the Oosterhoff effect in the stellar halo and difference in the radial distribution of the two Oosterhoff components is real, we performed a series of tests to examine systematic effects that might account for the difference. It appears that this result is robust.

Period Errors— Let us assume that the stellar halo consists of solely an OoI population of RR Lyrae stars. Is it possible that OoI RR Lyrae stars might be misidentified as OoII? For example, it is possible that periods are grossly mis-estimated. Could our timeseries analysis and detection process artificially produce an OoII population? We simulated RR Lyrae light curves with period and amplitude distributions of OoI and OoII RR Lyrae stars. These simulated RR Lyrae light curves were processed through our detection pipeline, which was described in the previous section, and used in the selection of final LONEOS - I RR Lyrae sample discussed in this section. Figure 23 shows the period shift histograms for one field with 28 images (1374B). We have scaled the OoII input sample to contain 26% of the OoI component, which is what we observe in the LONEOS - I sample. The detection process tends to broaden the period shift distributions and produces long tails. However, the OoI and OoII components are still recognizable.

Efficiency— In order to calculate the RR Lyrae star number density, we need to estimate the detection efficiencies. This was described in the previous section. In calculating the detection efficiencies, we averaged over the period and amplitude distributions from previous surveys. These distributions are essentially for the Oosterhoff I class. The assumption that we have made is that the detection efficiencies for OoI and OoII are identical. In order to investigate differences in the detection efficiencies, we simulate RR Lyrae light curves to

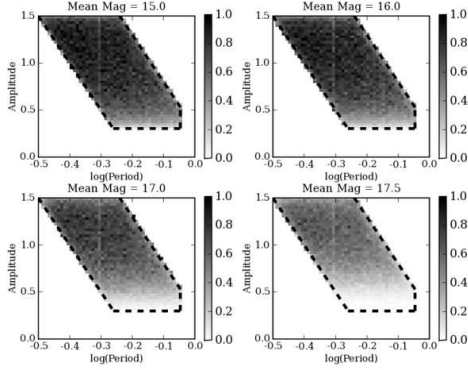


FIG. 24.— The detection efficiency in period-amplitude space for fields with less than 30 images, which are fields with the fewest images. We simulated 310,000 RR Lyrae stars with mean magnitude of 17.0. Note that color table has been inverted (i.e., black corresponds to 100% efficient). We did not find any dependence of the efficiency with period at a fixed amplitude. Also, one can see a deficiency at a period of 0.5 days (-0.3 on the log scale), which is caused by the window function of these fields.

explore the detection efficiencies in the period-amplitude space. We performed more extensive simulations examining only fields with less than 30 images, which are fields with the fewest images and represent the worst-case scenario. We simulated 310,000 RR Lyrae stars with mean magnitudes of 15, 16, 17, & 17.5 (Figure 24). There is a strong trend with amplitude which is expected given the photometric error trend with magnitude. We also observe a deficiency near a period of 0.5 days (-0.3 on the log scale), which is caused by the sampling window function of these fields. We find no dependence of the efficiency with period at fixed amplitude. Thus, we are confident that the efficiency differences do not account for the difference in the radial distributions of the OoI and OoII components.

What effect could an error in the detection efficiency have? We have measured the power law indices for two Oosterhoff components without including the detection efficiency correction. This yields the following fits:

$$\rho_{OoI} \sim R^{-2.68 \pm 0.06}, \quad (28)$$

$$\rho_{OoII} \sim R^{-3.17 \pm 0.1}. \quad (29)$$

The detection efficiency correction tends to make the distributions shallower. Even if we take the extreme scenario where our detection efficiency correction is only applied to the OoII component and we assume that the OoI component has a 100% detection efficiency, the difference in the radial distributions of the Oosterhoff components remains statistically significant.

Color Differences— Is it possible to explain the OoI and OoII difference because of color difference? Does the photometric calibration introduce a bias based on color? We looked to see if our OoI and OoII components have different color distributions. First, we have acquired dereddened 2MASS colors for several hundred of the LONEOS - I RR Lyrae stars. Figure 25 show the color distributions for each Oosterhoff component. The distributions appear to be consistent and no infrared color difference is seen. In addition, Figure 26 shows the color

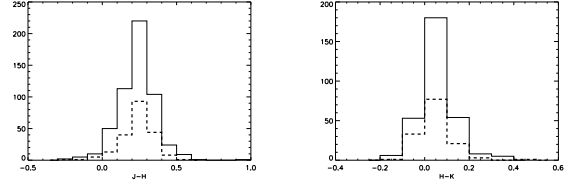


FIG. 25.— 2MASS colors for the OoI and OoII components. There is no significant color difference between the two components.

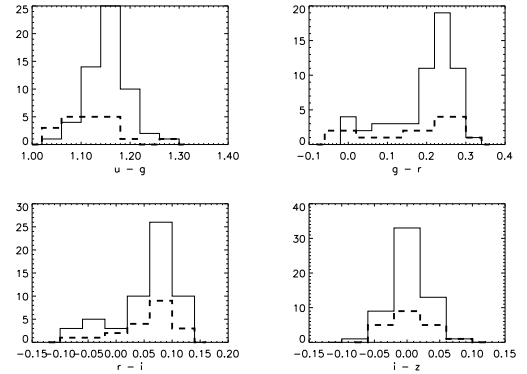


FIG. 26.— SDSS color distributions for LONEOS - I RR Lyrae stars (78). The Oo I component is shown as the solid curve, while the Oo II component is shown as a dashed line.

distributions for the 78 RR Lyrae stars with SDSS DR3 photometry. While this sample is small, we do not see major differences in the SDSS colors of the LONEOS - I RR Lyrae stars, except for the $u - g$ color, where the OoI component appears to be bluer. This $u - g$ color difference could be due to a difference in metallicity.

Zeropoint Differences— Zeropoint differences between the two Oosterhoff components may arise in several forms: absolute magnitude differences, photometric zeropoint offsets, and mean magnitudes errors. First, we explore whether the difference in the radial distribution of the OoI and the OoII components could result from intrinsically different absolute magnitudes. In Figure 27, we show the dependence of the power law exponent on the absolute magnitude for the two Oosterhoff components. If we fix the absolute magnitude of the OoI stars to $M_V = 0.71$, this would require that the absolute magnitude of the OoII component be roughly $M_V \geq 1.5$ in order to have the same power law slope. This value is not within the observed range of M_V for RR Lyrae of any kind. Thus, an absolute magnitude difference between the OoI and OoII components cannot explain the different radial distributions.

Does the photometric calibration introduce a bias based on color? Even though we do not see a clear color difference between the Oosterhoff components, let us explore how a difference could affect our results. As we saw in Section 2 (Figure 2), the offset from LONEOS - I magnitudes (tied to GSC2 F) to V_{SDSS} is a function of color. A systematic error in this offset directly translates to a systematic offset in the mean magnitudes (and distances) of all the RR Lyrae stars. This will lead to different radial profiles. We have used an offset for a color range of RR Lyrae stars. Figure 2 indicates that the offset may vary by ~ 0.3 at the extremes of the RR

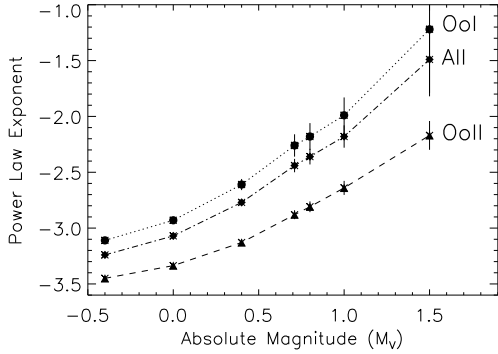


FIG. 27.— The dependence of the power law exponent on the RR Lyrae absolute magnitude for the entire LONEOS-I RR Lyrae sample, OoI and OoII components is shown. If we fix the absolute magnitude of the OoI stars to $M_V = 0.71$, this would require that the absolute magnitude of the OoII component be roughly $M_V > 1.5$. This value is not within the observed range of M_V for RR Lyrae of any kind. Thus, an absolute magnitude difference between the OoI and OoII components cannot explain the different radial distributions.

Lyrae color range. To give us an idea of how this affects the radial profiles of the Oosterhoff components, let us look at Figure 27, where we explore how changes in the absolute magnitude affect the radial distributions. An overall shift in the LONEOS - I zeropoint is essentially changing the RR Lyrae absolute magnitude. If we fix M_V and assume the two Oosterhoff components have a 0.2 mag overall zeropoint difference, this can not explain the difference in the two radial distributions. One needs an overall zeropoint difference of ~ 1 mags, which we are confident does not exist.

It is possible that intrinsic light curve shape differences in the OoI and OoII components could result in a systematic bias in the mean magnitudes of the OoI and OoII components. Any systematic difference in the measured mean magnitude is a zeropoint offset. However, Figure 27 shows that the mean magnitude bias would have to be a sizable fraction of the RR Lyrae amplitude and thus unrealistic that the radial profiles could result from a bias in the measure of the mean magnitudes.

Spatial Sub-Samples— We have divided the LONEOS - I RR Lyrae sample into regions above and below the Galactic plane. This division roughly divides the entire sample in half (372 and 466, above and below the plane, respectively). Figure 28 shows the spherically symmetric radial distributions for the entire sample as well as for the OoI and OoII components (see also Table 4). The OoII component’s profiles are consistent with the full OoII sample. However, the OoI shows a 2.8σ difference above and below the Galactic plane with power law exponents of -2.61 ± 0.09 and -2.16 ± 0.13 , respectively. If this difference is real, it could indicate spatial asymmetries in the OoI component. However, the above and below plane difference in power law slope is of marginal statistical significance. We are engaged in the analysis of the LONEOS II data set which (with its much greater sky coverage) should lay this issue to rest one way or another. It is also possible that this difference is caused by some systematic variation in the LONEOS - I photometric completeness function which we have not taken into account. Recall, that we use a global photometric

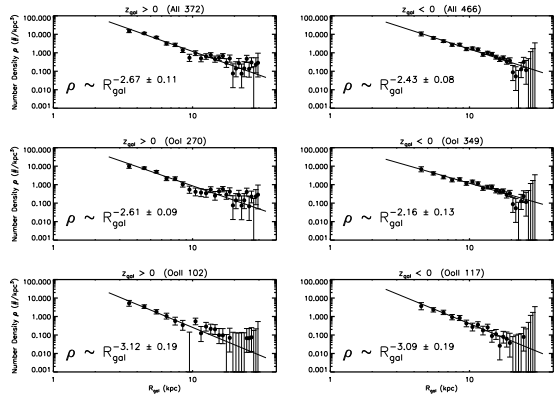


FIG. 28.— We have divided the LONEOS - I RR Lyrae sample into regions above and below the Galactic plane. This figure shows the spherically symmetric radial distributions for the entire sample as well as for the OoI and OoII components. The OoII component’s profiles are consistent with the full OoII sample. However, the OoI shows a 2.8σ difference above and below the Galactic plane with power law exponents of -2.61 ± 0.09 and -2.16 ± 0.13 . If this difference is real, it could indicate spatial asymmetries in the OoI component. However, the above and below plane difference in power law slope is of marginal statistical significance.

TABLE 4
POWER LAW FITS ABOVE AND BELOW THE GALACTIC DISK

| Location | Sample (Size) | Exponent |
|---------------|---------------|------------------|
| $z_{gal} > 0$ | All (372) | -2.67 ± 0.11 |
| $z_{gal} < 0$ | All (466) | -2.43 ± 0.08 |
| All | All (838) | -2.43 ± 0.06 |
| $z_{gal} > 0$ | OoI (270) | -2.61 ± 0.09 |
| $z_{gal} < 0$ | OoI (349) | -2.16 ± 0.13 |
| All | OoI (619) | -2.26 ± 0.07 |
| $z_{gal} > 0$ | OoII (102) | -3.12 ± 0.19 |
| $z_{gal} < 0$ | OoII (117) | -3.09 ± 0.19 |
| All | OoII (219) | -2.88 ± 0.11 |

completeness function for LONEOS - I and a field-by-field temporal completeness correction. We have investigated if there was a systematic difference between the LONEOS - I fields above and below the Galactic plane. First, we derived a photometric completeness function for the LONEOS - I fields above and below the plane using SDSS Data Release 5. Using the same criteria that we used to obtain the global photometric completeness function (Figure 13), we queried the LONEOS - I database for a detection in each image in the database and computed photometric completeness functions above and below the Galactic Plane. There were about one million detections of SDSS DR5 stars in the LONEOS - I database above and below the Galactic Plane. However, we did not find a significant difference between photometric completeness functions above and below the Galactic Plane. Next, we performed lightcurve simulations, like those in Figure 24, to compare the temporal detection efficiency in the period-amplitude space for LONEOS - I fields above and below the Galactic plane. Again, no significant difference was seen for the fields above and below the Galactic plane. However, the OoI and OoII still have different profiles in each hemisphere, but the extent of the difference is not presently clear.

CCD Focal Plane Distribution— In order to obtain the wide field of view needed for LONEOS, the telescope used has a Schmidt design. A Schmidt telescope consists of a spherical primary mirror and a corrector lens

at its radius of curvature. However, distortions in the focal plane persist. These distortions increase near the edges of the focal plane (i.e., with increased distance from the optical axis). Such distortion might affect the amplitude of our RR Lyrae stars. We examined the distribution of our RR Lyrae stars in the CCD focal plane to search for any unusual clustering that might result from the optical distortions. We use an extension of a one-dimensional Kolmogorov-Smirnov test to two-dimensions (Press et al. 1992). We find that the RR Lyrae distribution is not significantly different from a random 2D distribution. In addition, we examine the distributions of the two Oosterhoff components. The KS probability indicates that these distributions are not significantly different from one another.

Large Amplitude Sample— The detection efficiency generally decreases with decreasing amplitude. We examined the radial distributions of the OoI and OoII components while restricting the sample to include only RR Lyrae stars with amplitudes greater than 0.6. The difference in the radial distributions of the two components remains unchanged.

Increased Cadence Subsample— Finally, we look at a subsample selected from fields with more than 32 epochs. Such a subsample should be less affected by efficiency differences. This results in 370 OoI and 129 OoII RR Lyrae stars. The power law exponents are $\alpha = -2.46 \pm 0.1$ and $\alpha = -2.95 \pm 0.14$ for the OoI and OoII components, respectively. Again, the difference in radial distributions remains.

5.2. Implications for Galactic Formation

The first serious model of galaxy formation was proposed by Eggen et al. (1962) (ELS). Based on correlations between metallicity, orbital eccentricity, angular momentum, and velocity perpendicular to the Galactic Plane in a sample of nearby, high velocity (halo) field stars, they concluded that the Galaxy formed from the rapid (within the free fall time), monolithic collapse of an overdensity in the primordial density field. The first stars that formed during the collapse inherited the low metallicity and predominantly radial motion of the collapsing gas, while conservation of angular momentum and energy dissipation led to the formation of a flattened and circularly rotating thin disk of gas. Metal-rich stars would form in this disk as the interstellar medium became enriched with the products of nucleosynthesis during stellar evolution.

There has been mounting evidence to suggest that the ELS scenario does not agree with observations. Searle & Zinn (1978) (SZ) presented an extensive survey of globular clusters in the outer halo that showed a spread in their horizontal branch (HB) morphology (i.e., color distribution of stars along the HB) that is independent of metallicity, the “second parameter problem”. This effect was not evident in clusters with smaller galactocentric distances. SZ proposed that age was the second parameter and that the outer clusters originated in satellite systems that were subsequently accreted by the Milky Way. The spread in HB morphology can be explained by different star formation histories in the accreted systems. Today, the most successful large-scale structure formation models are based on hierarchical clustering (i.e., the

Cold Dark Matter (CDM) paradigm). The SZ scenario for galaxy formation is attractive since it would fit within the CDM paradigm of structure formation. Several accreted systems have been detected in the Milky Way (e.g., Ibata et al. 2001; Belokurov et al. 2007), which would provide direct support for SZ scenario.

In studies of globular cluster RR Lyrae stars, the location of an RR Lyra star in period-amplitude space has been correlated to metallicity (e.g., Sandage 1993; Contreras et al. 2005) and age relative to the Zero-Age Horizontal Branch (ZAHB) (e.g., Lee et al. 1990; Clement & Shelton 1999). Clement & Shelton (1999), Lee & Carney (1999), and Jurcsik et al. (2003) conclude that the Oosterhoff effect is caused by evolution off the ZAHB. They found that OoII globular clusters are not correlated with metallicity, but rather their RR Lyrae stars appear to have evolved off the ZAHB. Relative age estimates between the OoI and OoII globular cluster populations are 2-3 Gyr (Lee & Carney 1999). Lee & Carney (1999) have found that the kinematic properties of OoI and OoII globular clusters are different. They found that the OoI clusters have little or no net angular momentum, which points to a formation scenario like that of SZ. On the other hand, OoII clusters were found to have a net prograde rotation ($V_{rotation} = -94 \pm 47$ km/s), which indicates that their formation scenario resembles the ELS scenario. The kinematic data and the relative age differences (indicated by the Oosterhoff type) of OoI and OoII clusters point to a dual mode formation scenario for the globular clusters.

Our detection of the Oosterhoff effect in the Galactic stellar halo indicates that the formation of the globular clusters may be connected to that of the Galactic stellar halo. If the Oosterhoff type indicates an age difference, then the Oosterhoff effect in the stellar halo suggests a time gap between the formation of the OoI and OoII components. It should be noted that an age difference between OoI and OoII components does not give us any information about when the OoI component may have been accreted into the Milky Way. However, the presence of the two distinct components in the stellar halo discovered in LONEOS - I indicates that the progenitors of the stellar halo had diverse ages and/or chemical properties.

One way to connect the OoI and OoII components to the ELS and SZ scenarios would be to search for phase-space substructure. First, if the OoI component was formed predominantly in the SZ scenario than we would expect the stellar halo to have over- and under-densities. While there has been much excitement concerning the discovery of the overdensities in the stellar halo that are associated with accreted systems, the stellar halo should also have voids or underdensities if it was formed in an SZ scenario. The radial distributions of both components exhibit no significant substructure. However spatial substructure tends to be quickly erased. Thus, the lack of substructure in the OoI component may simply indicate that the number of accretions in the past 1-2 Gyrs has been low. In addition, LONEOS - I probes a small fraction of the Galactic Halo. A much larger survey is needed to explore whether there are differences in the amount of substructure in the OoI and OoII components.

Besides the possible time gap between the formation of the OoI and OoII components, the difference in the ra-

dial distributions of the OoI and the OoII components is suggestive of multiple physical mechanisms for the formation of the stellar halo. If one assumes that the Galactic stellar halo was formed by a combination of ELS and SZ scenarios, then one might associate the two Oosterhoff components of the stellar halo to each of those scenarios. The relatively steeper radial distribution of the OoII component as compared to the OoI component could be a manifestation of the fact that an ELS scenario is more dissipative than an SZ scenario. An ELS scenario would be more dissipative since there is much gas in the system. Loss of energy (e.g., from radiative transfer phenomena) would result in a contraction of the halo. Whether the contraction was isotropic or not depends on the amount of angular momentum in the system.

However, our detection of the Oosterhoff effect in the stellar halo does not necessarily imply that the stellar halo was formed through a combination of ELS and SZ scenarios. It might be able to form two radially distinct population of RR Lyrae stars through a combination of hierarchical mergers which could have been dissipative and dissipationless (e.g., Bekki & Chiba 2001; Chiba & Beers 2000). It is possible that systems accreted at early times contained considerable gas, and would have resulted in dissipative merging. However, systems accreted at later times would have contained less gas due to star formation and ejection from supernovae explosions. This late-time merging would have resulted in dissipationless merging. Using a large sample of stellar spectra, Carollo et al. (2007) found that the stellar halo is composed of at least two spatially, kinematically, and chemically distinct components, which agrees with our results. Carollo et al. (2007) argue that their data can be explained solely within the context of hierarchical merging. This scenario could account for the two spatially distinct components in the LONEOS - I sample as well.

We have found that the stellar halo is predominately OoI, with a significant OoII component. We cannot rule out whether the stellar halo contains an intermediate Oosterhoff class. Siegel (2006) and Dall’Ora et al. (2006) have found that the recently discovered Boötes dSph galaxy to be of OoII type. Since the Boötes dSph is metal-poor and is an OoII, it supports the argument that the Oosterhoff effect is a continuous effect which is predominately associated with metallicity. This new finding raises the possibility the OoII component of the Galactic stellar halo was formed from accreted systems like Boötes.

The chemical abundance properties of the stellar halo and the dwarf galaxies are distinct (e.g., Venn et al. 2004). The stellar halo is more metal-poor, but with enhanced $[\alpha/Fe]$ abundances, than the Local Group dwarf galaxies. Robertson et al. (2005) have shown that such a discrepancy can be explained within the CDM paradigm. Using cosmologically-motivated star formation and gas accretion histories, they argue that most of the stellar halo was formed from short-lived satellites which were accreted and destroyed at early times. Since these early progenitor satellites were short-lived, there is limited time for stellar enrichment and the dominant contributor to the enrichment is from Type II supernovae (i.e., α -enrichment). However, the present day Local Group dwarf galaxies have had a long time to produce metals

from both Type I and II supernovae. The bottom line is that the dwarf galaxies that we observe in the Local Group may not be representative of the progenitors of the stellar halo. A detailed study of metallicity of the two Oosterhoff halo components will allow us determine if there is an age difference between these two Oo components.

6. CONCLUSIONS

We present a catalog of 838 *ab*-type RR Lyrae in the Galactic stellar halo from the LONEOS - I survey. We find evidence for two distinct components in this sample. We associate these two components with a manifestation of the Oosterhoff effect in the stellar halo. In addition, we find that these two components have significantly different radial distributions. Without flattening, the OoI has a power-law exponent of -2.26 ± 0.1 while the OoII component has a significantly steeper slope with -2.88 ± 0.04 . The flattening of the halo cannot be constrained by this data set since the distribution on the sky is limited. We performed numerous tests and simulations to verify the existence of the two components and their difference in their Galactocentric radial distributions. Our finding is robust with respect to potential systematic errors due to e.g. detection efficiencies, zeropoint problems, color differences, camera systematics, etc. It is likely that the OoII component potentially represents an older population and traces an early dissipative collapse or early dissipative merging activity. The OoI component represents the later accretion of younger systems. Spectroscopic data would be very valuable, the radial velocities will tell us if these OoI and OoII components have different kinematic properties and occupy different regions in phase-space. Spectroscopic data could also supply evidence for chemical differences. Chemical differences in these two populations will give us information regarding the environment and age of these populations.

In 2000, the LONEOS camera (LONEOS - II) was upgraded, and now consists of two 2k x 4k backside-illuminated CCDs, giving it an 8.1 square degree FOV (2.8 arcsec/pixel), and reaches to a depth of $R \sim 19.3$. Approximately one quarter of the sky is covered with more than 40 epochs of measurements. Photometric reduction and analysis of the new camera data has commenced, and results will be discussed in future papers. The LONEOS - II data should also increase our RR Lyrae sample by an order of magnitude with a wider and deeper survey area. The data from the LONEOS - II camera will produce cleaner period-amplitude distributions. This will be enable us to search for additional “fine structure” in the period-amplitude distribution.

7. ACKNOWLEDGMENTS

AR is grateful to the NOAO Goldberg fellowship program for its support. CWS is grateful for the support from the Packard Foundation that was essential to the success of this project. CWS and AM are also grateful to Harvard University for their support. KHC’s work was performed under the auspices of the U.S. Department of Energy, National Nuclear Security Administration by the University of California, Lawrence Livermore National Laboratory under contract No. W-7405-Eng-48. Conversations with Scott Anderson, Al Diercks, Steven Majewski, Gajus Miknaitis, Nick Suntzeff, George Waller-

stein, and Doug Welch provided encouragement, insight and motivation for this work. We also acknowledge the anonymous referee's comments which made this a better paper. The LONEOS project is supported by the Lowell Observatory and NASA grant NAGW-3397. This research has made use of the SIMBAD database, operated at CDS, Strasbourg, France. Simulations in this paper were performed with the use of Condor, high-throughput distributed computing system at the University of Washington. The Condor Software Program (Condor) was developed by the Condor Team at the Computer Sciences Department of the University of Wisconsin-Madison. All rights, title, and interest in Condor are owned by the Condor Team (<http://www.cs.wisc.edu/condor/>).

REFERENCES

- Abazajian, K., et al. 2005, *AJ*, 129, 1755
- Alcock, C., et al. 2000, *ApJ*, 542, 257
- Alcock, C., et al. 1998, *ApJ*, 492, 190
- Alcock, C., et al. 1995, *AJ*, 109, 1653
- Bekki, K., & Chiba, M. 2001, *ApJ*, 558, 666
- Belokurov, V., et al. 2007, *ApJ*, 654, 897
- Benedict, G. F., et al. 2002, *AJ*, 123, 473
- Bowell, E., Koehn, B. W., Howell, S. B., Hoffman, M., & Muinonen, K. 1995, *Bulletin of the American Astronomical Society*, 27, 1057
- Cacciari, C., Corwin, T. M., & Carney, B. W. 2005, *AJ*, 129, 267
- Carney, B. W., Fulbright, J. P., Terndrup, D. M., Suntzeff, N. B., & Walker, A. R. 1995, *AJ*, 110, 1674
- Carollo, D., et al. 2007, *astro-ph/07063005*
- Catelan, M. 2006, *astro-ph/0604035*
- Chiba, M., & Beers, T. C. 2000, *AJ*, 119, 2843
- Clement, C. M., et al. 2001, *AJ*, 122, 2587
- Clement, C. M., & Shelton, I. 1999, *ApJ*, 515, L85
- Contreras, R., Catelan, M., Smith, H. A., Pritzl, B. J., & Borissova, J. 2005, *Astrophys. J.*, 623, L117
- Dall’Ora, M., et al. 2006, *ApJ*, 653, L109
- Diercks, A. H., Angione, J., Stubbs, C. W., Cook, K. H., Bowell, E., Koehn, B. W., Nye, R. A., & Dodgen, D. 1995, in *Proc. SPIE Vol. 2416*, p. 58-64, *Cameras and Systems for Electronic Photography and Scientific Imaging*, Constantine N. Anagnostopoulos; Michael P. Lesser; Eds., 58
- Eggen, O. J., Lynden-Bell, D., & Sandage, A. R. 1962, *ApJ*, 136, 748
- Gehrels, N. 1986, *ApJ*, 303, 336
- Hawkins, M. R. S. 1984, *MNRAS*, 206, 433
- Heck, A. 1988, *A&AS*, 75, 237
- Ibata, R., Lewis, G. F., Irwin, M., Totten, E., & Quinn, T. 2001, *ApJ*, 551, 294
- Ivezić, Ž., et al. 2000, *AJ*, 120, 963
- Ivezić, Ž., Vivas, A. K., Lupton, R. H., & Zinn, R. 2005, *AJ*, 129, 1096
- Jurcsik, J., Benkő, J. M., Bakos, G. Á., Szeidl, B., & Szabó, R. 2003, *ApJ*, 597, L49
- Kinemuchi, K., Smith, H. A., Woźniak, P. R., & McKay, T. A. 2006, *AJ*, 132, 1202
- Kinman, T. D., Wirtanen, C. A., & Janes, K. A. 1966, *ApJS*, 13, 379
- Krisciunas, K. 2001, Ph.D. Thesis (University of Washington)
- Krisciunas, K., Margon, B., & Szkody, P. 1998, *PASP*, 110, 1342
- Layden, A. C. 1995, *AJ*, 110, 2288
- Layden, A. C. 1998, *AJ*, 115, 193
- Layden, A. C., Hanson, R. B., Hawley, S. L., Klemola, A. R., & Hanley, C. J. 1996, *AJ*, 112, 2110
- Lee, J., & Carney, B. W. 1999, *AJ*, 118, 1373
- Lee, Y., Demarque, P., & Zinn, R. 1990, *ApJ*, 350, 155
- Oort, J. H., & Plaut, L. 1975, *A&A*, 41, 71
- Oosterhoff, P. T. 1939, *The Observatory*, 62, 104
- Press, W. H., Teukolsky, S. A., Vetterling, W. T., & Flannery, B. P. 1992, *Numerical recipes in C. The art of scientific computing* (Cambridge: University Press, —c1992, 2nd ed.)
- Preston, G. W., Shectman, S. A., & Beers, T. C. 1991, *ApJ*, 375, 121
- Reid, N., & Hawley, S. L. 2000, *New light on dark stars : red dwarfs, low mass stars, brown dwarfs* (Springer-Praxis series in astronomy and astrophysics 2000)
- Reimann, J. D. 1994, Ph.D. Thesis (University of California)
- Rest, A. 2002, Ph.D. Thesis (University of Washington)
- Robertson, B., Bullock, J. S., Font, A. S., Johnston, K. V., & Hernquist, L. 2005, *ApJ*, 632, 872
- Saha, A. 1985, *ApJ*, 289, 310
- Sandage, A. 1993, *AJ*, 106, 687
- Sandage, A., Katem, B., & Sandage, M. 1981, *ApJS*, 46, 41
- Scargle, J. D. 1982, *ApJ*, 263, 835
- Schechter, P. L., Mateo, M., & Saha, A. 1993, *PASP*, 105, 1342
- Schlegel, D. J., Finkbeiner, D. P., & Davis, M. 1998, *ApJ*, 500, 525
- Searle, L., & Zinn, R. 1978, *ApJ*, 225, 357
- Siegel, M. H. 2006, *astro-ph/0607091*
- Smith, H. A. 1995, *RR Lyrae stars* (Cambridge Astrophysics Series, Cambridge, New York: Cambridge University Press, 1995)
- Space Telescope Science Institute, ., & Osservatorio Astronomico di Torino. 2001, *VizieR Online Data Catalog*, 1271, 0
- Stellingwerf, R. F. 1978, *ApJ*, 224, 953
- Suntzeff, N. B., Kinman, T. D., & Kraft, R. P. 1991, *ApJ*, 367, 528
- Venn, K. A., Irwin, M., Shetrone, M. D., Tout, C. A., Hill, V., & Tolstoy, E. 2004, *AJ*, 128, 1177
- Vivas, A. K., & Zinn, R. 2006, *astro-ph/0604359*
- Vivas, A. K., Zinn, R., et al. 2004, *AJ*, 127, 1158
- Wetterer, C. J., & McGraw, J. T. 1996, *AJ*, 112, 1046
- Zinn, R. 1985, *ApJ*, 293, 424